CMS Physics Analysis Summary

Proton reconstruction with the CMS Precision Proton Spectrometer in Run 2

The CMS and TOTEM Collaborations

Abstract

The Precision Proton Spectrometer of the CMS experiment (PPS) collected more than 110 fb^{-1} of data over the course of the LHC Run 2. This note illustrates the key features of the PPS alignment and optics calibrations developed during this period, the proton reconstruction procedure as well as the detector efficiency and the performance of the PPS simulation. The reconstruction and simulation are validated using a sample of (semi-)exclusive di-lepton events.

Contents

1 Introduction

The Precision Proton Spectrometer (PPS) detector system has been installed and integrated into the CMS experiment [1] during the LHC Run 2. It is a joint project of the CMS and TOTEM [2] collaborations with the capability of measuring protons scattered at very small angles at high instantaneous luminosity [3]. The scattered protons that remain inside the beam pipe, displaced from the central beam orbit, can be measured by detectors placed inside movable beam pipe insertions, called Roman pots (RP), which approach the beam down to a few mm. The PPS detectors have collected data corresponding to an integrated luminosity larger than $110 \, \mathrm{fb}^{-1}$ during the LHC Run 2, between 2016 and 2018.

The physics motivation behind PPS is the study of central exclusive production (CEP), i.e. the process $\mathrm{pp} \rightarrow \mathrm{p}^{(*)} + \mathrm{X} + \mathrm{p}^{(*)}$ mediated by color-singlet exchanges (photons, Pomerons, Z bosons), by detecting at least one of the outgoing protons. In CEP, one or both protons may dissociate into a low-mass state ($\mathrm{p}^{(*)}$); dissociated protons do not produce a signal in PPS. The X system is produced at central rapidities, and its kinematics can be fully reconstructed from the 4-momenta of the protons, thereby giving access to standard model (SM), or beyond SM (BSM) final states that are otherwise difficult to observe in the CMS central detectors because of the large pileup at high luminosities. CEP provides unique sensitivity to SM processes in events with Pomeron and/or photon exchange, and BSM physics, e.g. via searches for anomalous quartic gauge couplings, axion-like particles, and in general new resonances [4–8].

This note is organized as follows. The CMS detector and PPS are described in Section 2. The LHC optics and the concept of proton transport is presented in Section 3, followed by a description of the datasets used in Section 4. Sections 5 and 6 describe the detector alignment procedure and the LHC optics calibration. Section 7 details the proton reconstruction with the PPS detectors. Sections 8 and 9 document the study of LHC aperture limitations and the simulation of the proton transport and PPS detectors, while Section 10 describes the uncertainties affecting the proton reconstruction. A validation of the reconstruction using a (semi)exclusive dimuon sample is presented in Section 11. The measurement of the proton reconstruction efficiency is discussed in Section 12. Section 13 describes a study of the performance of the proton vertex matching criteria from time-of-arrival measurements. Finally, a summary is presented in Section 14.

2 The CMS detector and PPS

The central feature of the CMS apparatus is a superconducting solenoid of 6 m internal diameter, providing a magnetic field of 3.8 T. Within the solenoid volume are a silicon pixel and strip tracker, a lead tungstate crystal electromagnetic calorimeter, and a brass and scintillator hadron calorimeter, each composed of a barrel and two endcap sections. Forward calorimeters extend the pseudorapidity coverage provided by the barrel and endcap detectors. Muons are measured in gas-ionization detectors embedded in the steel flux-return yoke outside the solenoid.

Events of interest are selected using a two-tiered trigger system. The first level (L1), composed of custom hardware processors, uses information from the calorimeters and muon detectors to select events at a rate of around 100 kHz within a fixed latency of about 4 μs [9]. The second level, known as the high-level trigger (HLT), consists of a farm of processors running a version of the full event reconstruction software optimized for fast processing, and reduces the event rate to around 1 kHz before data storage [10].
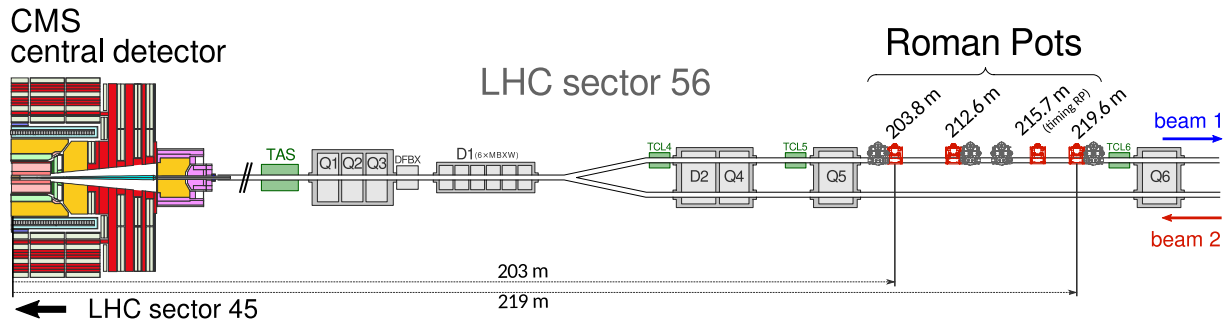
Figure 1: Schematic layout of the beam line between the interaction point and the RP locations in LHC sector 56, corresponding to the negative z direction in the CMS coordinate system and the outgoing proton in the clockwise beam direction. The accelerator magnets are indicated in grey and the collimator system elements in green. The horizontal RPs are marked in red. The vertical RP units are indicated in dark grey; they are part of the TOTEM experiment. The vertical RPs are not used during high luminosity data taking; nevertheless, they provide PPS with a reference measurement for the calibration and alignment of the detectors.

A more detailed description of the CMS detector, together with a definition of the coordinate system used and the relevant kinematic variables, can be found in Ref. [1].

The PPS detectors

Figure 1 shows the layout of the RP system installed at around 200–220 m from the CMS interaction point (IP5), along the beam line in the LHC sector between the interaction points 5 and 6, referred to as sector 56. A symmetric set of detectors is installed in LHC sector 45. Some RPs approach the beam vertically from the top and bottom, some horizontally. During standard machine operation, scattered protons undergo a large displacement in the horizontal direction and a small vertical displacement at the RP positions. The horizontal RPs are hence used. The vertical RPs are used in special configurations of the machine and in low luminosity proton-proton fills for the calibration and alignment of the detectors.

Each detector arm consists of two RPs instrumented with silicon *tracking* detectors that measure the transverse displacement of protons with respect to the beam, and one RP with *timing* detectors to measure their time-of-flight. The tracking RP closer to the IP is referred to as "near", the other as "far". Silicon strip sensors with a reduced insensitive region on the edge facing the beam were initially used [11]. Each RP hosted 10 silicon strip sensor planes, half at a $+45°$ angle and half at a $-45°$ angle with respect to the bottom of the RP. These sensors cannot sustain a large radiation dose and cannot identify multiple tracks in the same event. They have for this reason been gradually replaced by new 3D silicon pixel sensors: one RP (in each arm) during the 2017 data taking run and all tracking RPs in 2018 were instrumented with 3D pixel sensors. Each such RP hosts six 3D pixel sensor planes [3]. A summary of the RP configurations used in different years is provided in Table 1.

The difference between the proton arrival times in the detectors on both sides of the IP is used to reject background events with protons from pileup interactions, or beam-halo particles. Timing detectors were operational in 2017 and 2018, with four detector planes hosted in a single RP. They consisted of single- and double-sided single crystal chemical vapour deposition (scCVD) diamond sensor planes [12], and one plane of ultra-fast silicon sensors [13] during the 2017 data taking.

year	near tracking RP	far tracking RP	timing RP
2016	203.8 m (strips)	212.6 m (strips)	-
2017	212.6 m (strips)	219.6 m (pixels)	215.7 m
2018	212.6 m (pixels)	219.6 m (pixels)	215.7 m

Table 1: RP configurations in different years. The numbers represent the RP distances from the IP, the sensor technology is indicated in parentheses. The RP layout was always symmetric about the IP. There were always two tracking RPs per arm; the one closer to the IP is denoted as "near", the other as "far". In 2016 no timing RPs were used.

3   LHC optics and proton transport

PPS is a proton spectrometer which uses the LHC accelerator magnets between the interaction point (IP) and the RPs. Scattered protons are detected in the RPs after having traversed a segment of the LHC lattice containing 29 main and corrector magnets [14].

Since the protons that reach our detectors travel more than 200 m inside the vacuum pipe of the LHC and very close to the LHC beams we use the system usually employed to describe beams inside an accelerator. The trajectory of protons in the vicinity of the central orbit [15, 16] can be described as follows. The proton kinematics $\mathbf{d}$ at a distance s from the IP (e.g. at the RPs) is related to the proton kinematics at the IP, $\mathbf{d}^*$, via the transport equation:

$$\mathbf{d}(s) = T(s, \xi) \cdot \mathbf{d}^*. \tag{1}$$

The proton kinematics is described by $\mathbf{d} = (x, \theta_x, y, \theta_y, \xi)^T$, where (x, y) and (θ_x, θ_y) indicate the transverse position and angles; ξ denotes the fractional momentum loss

$$\xi = (p_{\text{nom}} - p)/p_{\text{nom}}, \tag{2}$$

where p_{nom} and p are the nominal beam momentum and the proton momentum, respectively [17, 18].

In exclusive reactions ξ can be used to assess the mass of the centrally produced state

$$M_X = \sqrt{s\xi_1\xi_2} \tag{3}$$

and its rapidity

$$y = \frac{1}{2} \log \frac{\xi_1}{\xi_2}. \tag{4}$$

The transport matrix

$$T(s, \xi) = \begin{pmatrix} v_x & L_x & m_{13} & m_{14} & D_x \\ \frac{dv_x}{ds} & \frac{dL_x}{ds} & m_{23} & m_{24} & \frac{dD_x}{ds} \\ m_{31} & m_{32} & v_y & L_y & D_y \\ m_{41} & m_{42} & \frac{dv_y}{ds} & \frac{dL_y}{ds} & \frac{dD_y}{ds} \\ 0 & 0 & 0 & 0 & 1 \end{pmatrix} \tag{5}$$

is defined in terms of the so-called optical functions ($v_x, L_x, D_x, m_{i,j}$ and their vertical counterpart) [19]. The definition of the relevant optical functions and their determination are described in Section 6. The optical functions depend on LHC parameters like the betatron function value
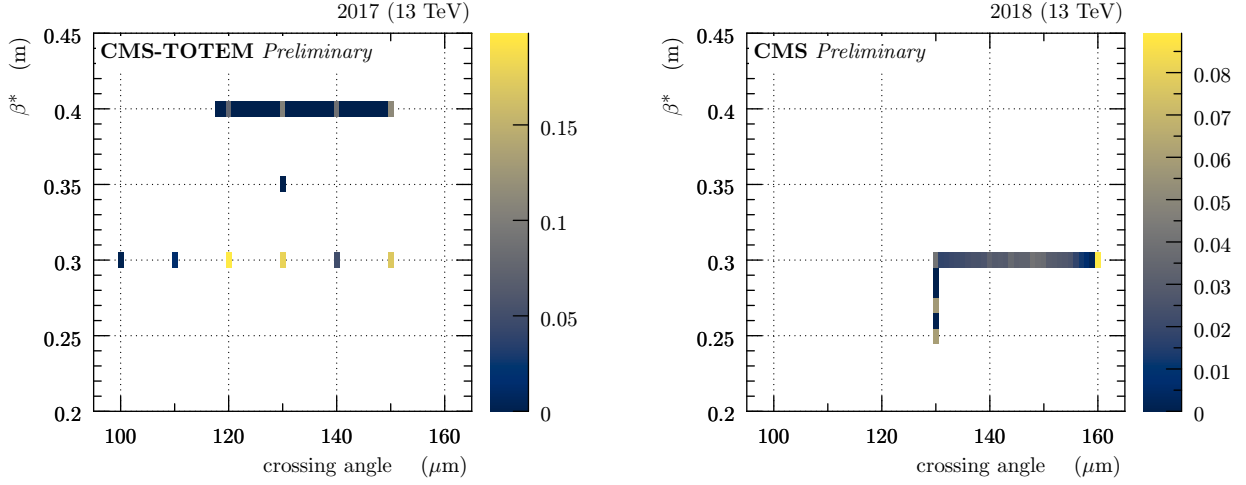
Figure 2: Frequency distributions of β^* vs. crossing angle configurations as extracted from data. **Left**: year 2017. **Right**: year 2018.

at the IP5 β^* and the crossing angle. Throughout this document, we refer to the half crossing angle, i.e. half the angle between the beams at their crossing point.

Figure 2 shows the distributions of β^* vs. crossing angle for the different data taking period ("physics fill") as extracted from data certified for analysis. In 2017, most of the data were recorded at four discrete values of the crossing angle: 150, 140, 130 and 120 μrad. The highest value was used at the beginning of the fills, then the crossing angle was reduced as the instantaneous luminosity dropped. β^* was set to 0.4 m (0.3 m) in periods before (after) Technical Stop 2 (TS2). In 2018, the crossing angle was changed continuously from 160 μrad at the beginning of the fill down to 130 μrad. Afterwards, β^* was changed in two discrete steps, from 0.3 to 0.27 and finally to 0.25 m. In 2016 (not shown in the figure) $\beta^* = 0.4$ m was used together with the crossing angle values of 185 μrad and 140 μrad for the pre-TS2 and post-TS2 periods, respectively.

4 Datasets

Two types of data are used for the calibration and alignment of the PPS detectors: data taken in high-intensity LHC "physics" fills and data taken in "alignment" fills, where the beam intensity is low. The different beam intensities are typically achieved by injecting different numbers of bunches in LHC, while the number of protons per bunch is almost the same, up to 1.2×10^{11}. The RP distances from the LHC beams are typically expressed in multiples of "beam sigmas", the RMS values of the beam transverse profile. The values of the beam sigma are the same for "alignment" and "physics" fills: $\sigma_{\text{beam}} \approx 0.1$ mm horizontally and $\sigma_{\text{beam}} \approx 0.4$ mm vertically.

The "physics" fills are standard LHC fills. There are up to 2500 bunches per beam, yielding instantaneous luminosity of about 10^{34} cm^{-2} s^{-1}. The average number of inelastic proton interactions at the IP (pileup) is typically in the range 15 to 55. Only horizontal RPs are inserted in these fills, to a distance of 15 σ_{beam}.

The "alignment" fills use the same LHC optics as the "physics" fills, but much lower beam intensity—typically only two bunches are injected per each beam. This gives instantaneous luminosities of the order of 10^{30} cm^{-2} s^{-1} and average pileup ≈ 20. The primary purpose of these fills is to establish the RP position with respect to the LHC collimators with a procedure
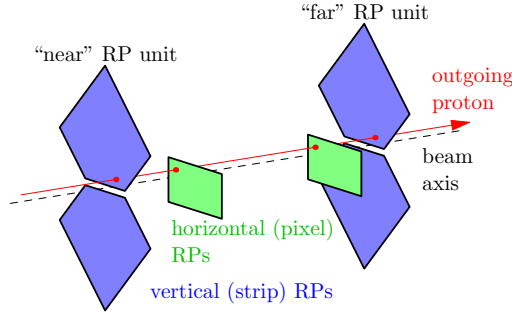
Figure 3: Overlap between vertical and horizontal RPs.

analogous to the LHC collimator alignment [20]. This is a precondition for systematic RP insertion close to the high-intensity LHC beams. Then, thanks to the low intensity, the safety rules allow to insert both horizontal and vertical RPs very close to the beam: at $6.5\,\sigma_{\mathrm{beam}}$ horizontally and at $5\,\sigma_{\mathrm{beam}}$ vertically. At these distances horizontal and vertical detectors overlap, as shown in Figure 3, which allows the relative alignment of the RPs in each arm. The presence of vertical RPs makes it possible to detect elastically scattered protons that are used for horizontal RP alignment with respect to the beam. The alignment procedure is detailed in Section 5. The very small distance of the horizontal RPs from the beam in the alignment fills permits to record additional data essential for optics calibration (cf. Section 6). There are typically two "alignment" fills per year of LHC operation.

The PPS datasets are divided in data taking periods. The PPS performance is often sensitive to the LHC settings (optics, collimators etc.) many of which vary with time—they are often changed during LHC technical stops (TS). For instance, the LHC optics was modified during the second technical stop (TS2) in 2016 and β^* was changed in TS2 in 2017. The technical stops are also occasions for updating the position of detectors in RP system. For example, in TS1 and TS2 in 2018, the tracking RPs were shifted vertically to distribute better the radiation dose accumulated by the pixel sensors. The sensor inefficiency due to radiation damage is discussed in Section 12. In Run 2, PPS was operated from 2016 to 2018. Table 2 summarises the PPS periods with significantly different LHC/RP settings and the corresponding integrated luminosities [21–23].

period	$L_{\mathrm{int}}(\,\mathrm{fb}^{-1})$
2016, pre-TS2	9.8
2016, post-TS2	5.0
2017, pre-TS2	15.0
2017, post-TS2	22.2
2018, pre-TS1	18.5
2018, TS1-TS2	26.8
2018, post-TS2	10.4
total	107.7

Table 2: List of PPS periods with distinct LHC and/or RP settings. L_{int} corresponds to the integrated luminosity recorded in runs certified for use in physics analysis.
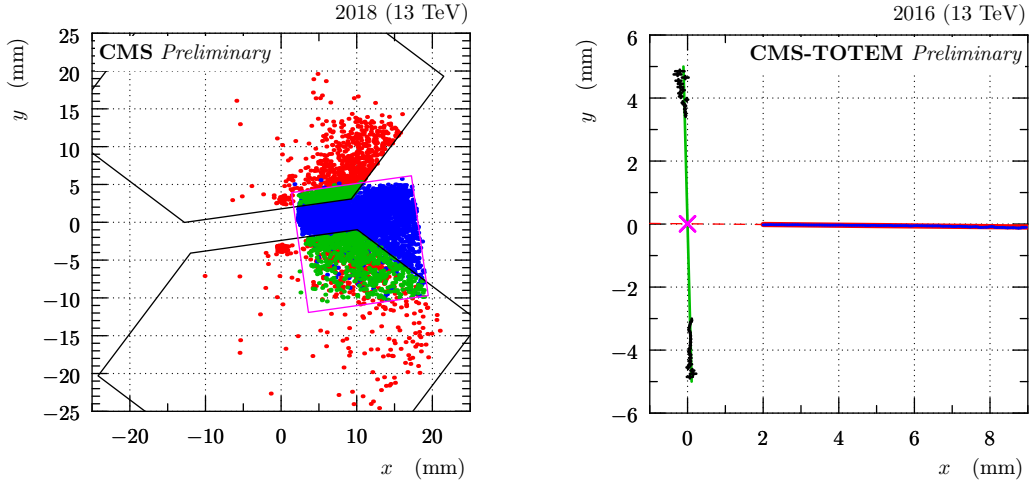
Figure 4: **Left**: relative alignment between vertical and horizontal RPs (April 2018). The plot shows track impact points in a scoring plane perpendicular to the beam. The points in red represent tracks only reconstructed from vertical RPs, in blue only from horizontal RPs and in green from both vertical and horizontal RPs. The size and position of the RP sensors is schematically indicated by the black (vertical strip RPs) and magenta (horizontal pixel RPs) contours. **Right**: determination of the beam position with respect to RPs (September 2016). Black: profile (mean x as a function of y) of elastic track impact points observed in vertical RPs; green: fit and interpolation. Blue: horizontal profile of minimum bias tracks found in the horizontal RP; red: fit and extrapolation. Magenta cross: the determined beam position.

5 Alignment

The alignment of RPs is a multi-level procedure including aligning sensor planes within each RP as well as aligning the RPs with respect to the LHC beam. This is one of the inputs for the proton reconstruction (discussed in detail in Section 7).

Although conceptually similar, the alignment of RPs is different from that of other CMS subdetectors. First, the RPs are movable devices – at the beginning of each LHC fill they are in a safe position away from the beam and are then inserted close to the beam only when the LHC reaches stable conditions. Second, the fill-to-fill beam position reproducibility has a limited accuracy. Consequently, it is desirable to determine the alignment parameters (at least) for every fill.

The alignment procedure involves multiple steps. A special "alignment" calibration LHC fill allows to determine the absolute position of the RPs with respect to the beam (Section 5.1). This calibration then serves as a reference for the alignment of every "physics" fill with standard conditions (Section 5.2). Once the tracking RPs are aligned with respect to the beam, the timing RPs are aligned with respect to the tracking RPs (Section 5.3).

5.1 Alignment fill

The "alignment" fill is a special LHC fill which allows to obtain data essential for calibration, not available in standard LHC "physics" fills (more details are given in Section 4).

The relative alignment – among sensor planes in all RPs and among all RPs in one arm – is determined by minimising residuals between hits and fitted tracks [24]. This is an iterative procedure since a priori it is not possible to distinguish between misalignments and outliers (unrelated hits due to noise etc.). Therefore the iteration starts with a large tolerance ($\mathcal{O}(100\,\mu\text{m})$, to
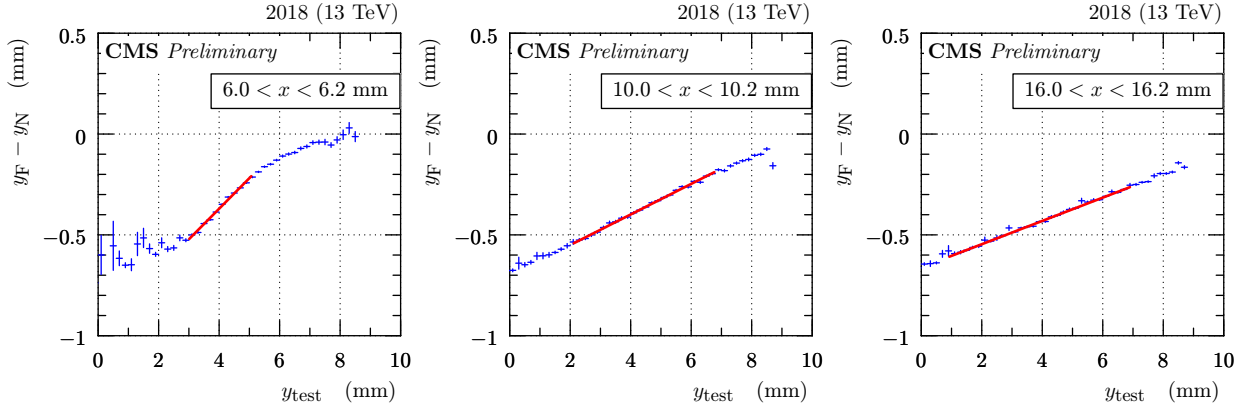
Figure 5: Illustration of $y_F - y_N$ dependence on y (fill 7139, 2018, near RP in sector 56). The three plots correspond to three x selections as indicated in the legends. Blue: profile histogram of the dependence, red: linear fit in the central part.

allow for misalignments) and as it proceeds the tolerance is decreased ($\mathcal{O}(10\,\mu\text{m})$, to gradually discard outliers). An illustration is shown in Figure 4, left, emphasizing the essential role of the overlap of the vertical and horizontal RPs. By construction, the relative alignment is not sensitive to misalignment modes that do not generate residuals, e.g. a global shift of the full RP system. These modes are addressed in the next step. The typical uncertainty of the relative RP alignment is few micrometres.

The vertical RPs can detect protons from elastic scattering, i.e. a process with only two protons in the final state, each having $\xi \equiv 0$ as a consequence of the momentum conservation. Because the two protons emerge from the same vertex with opposite directions, elastic events are relatively easy to tag (cf. Section 5.2.1 in Ref. [25]). Thanks to the azimuthal symmetry of the elastic scattering at the IP and the properties of the LHC optics, the elastic protons arrive at the RPs with impact points in the transverse plane elliptically distributed around the beam. Although only the tails of the elastic hit distributions are within the acceptance (protons with sufficiently large vertical scattering angle, $|\theta_y^*|$), the distributions can be used to extract the beam position with respect to the RPs. This is illustrated in Figure 4, right – the profile of the elastic hit distribution (black) is interpolated between the top and bottom RP (green), which provides information on horizontal alignment and potential rotations in the xy plane. This is combined with information from a minimum bias sample – most protons detected in horizontal RPs are due to pile up, thus unrelated to any trigger. The profile from the minimum bias sample (blue) is extrapolated linearly (red) to find the intersection (magenta cross) with the green line. The intersection indicates the beam position with respect to the RPs, with a typical uncertainty of about $10\,\mu\text{m}$.

5.2 Physics fills

For each high-luminosity LHC fill ("physics" fill), the horizontal RP alignment is obtained by matching observations from the fill to those from the reference "alignment" fill, cf. Section 5.1. Over time various matching metrics have been used (for some of the first choices see e.g. Ref. [26]), eventually converging to:

$$S(x) = \text{slope of profile } (y_F - y_N) \text{ vs. } y_{\text{test}}, \tag{6}$$

where y_N and y_F stand for the vertical track positions in the near and far RP, respectively. Similarly, y_{test} refers to the RP being aligned. The shape of the profile is illustrated in Figure
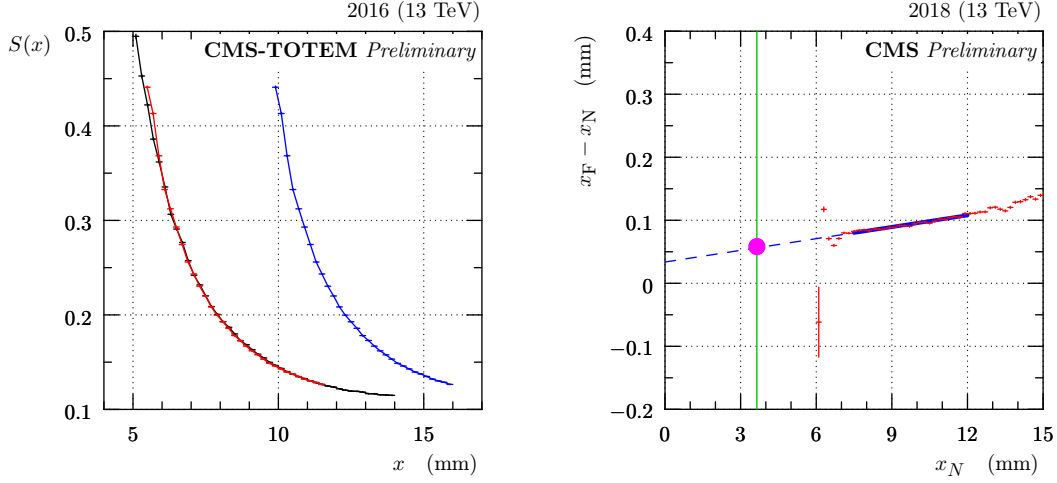
Figure 6: **Left**: illustration of absolute horizontal alignment (fill 5424, 2016 post-TS2, far RP in sector 45). Black: data from reference "alignment" fill, blue: data from a physics fill before alignment and red: data from the physics fill, aligned to match with the black reference. **Right**: illustration of horizontal near-far relative alignment (fill 7052, 2018 and sector 45). Red: mean value of $x_F - x_N$ as function of x_N. Blue: fit and extrapolation to the horizontal beam position (vertical green line, e.g. from the left plot). The value of the relative near-far alignment correction is indicated by the magenta dot.

5, where the value of S corresponds to the slope of the red line. The x dependence of the S function is generated by the LHC optics, cf. Section 6: y is mostly given by the vertical effective length, $L_y(\xi)$, and ξ is largely correlated with x because of the large horizontal dispersion, cf. Eq. (12). The optics has been verified to be stable in time and therefore $S(x)$ is suitable for matching observations between different fills. Furthermore, the function from Eq. (6) is convenient because of its slope character: vertical misalignments (shifts in y) cause no bias and unavailable parts of the phase space (e.g. because of localised radiation damage) do not have any detrimental impact since the slope can still be determined from the available part. The matching procedure is illustrated in Figure 6, left: the $S(x)$ curve from the test fill (blue) is shifted left and right until the best match with the $S(x)$ curve from the reference fill (aligned with the method from Section 5.1) is found. The shift between the blue and red curves is then used as the alignment correction.

The relative alignment between the RPs within the same arm is then refined with a dedicated method with a better sensitivity – good calibration of the relative alignment is essential for the multi-RP proton reconstruction, cf. Figure 37. The relative near-far alignment method is based on comparing horizontal track positions in the near and far RPs, x_N and x_F, respectively. The procedure is illustrated in Figure 6, right: the profile $x_F - x_N$ vs. x_N (red) is extrapolated (blue dashed) to the value of x_N corresponding to the beam position (green). The extrapolated value of $x_F - x_N$ (magenta dot) then gives the relative-alignment correction. In general, the $x_F - x_N$ difference can be generated either by misalignments (independent of the horizontal position) or by the optics (roughly proportional to horizontal displacement from the beam). The extrapolation to the beam position, where the displacement from beam is ≈ 0, thus suppresses the optics contribution and keeps the misalignment component only.

The vertical alignment is obtained by extrapolating (blue) the observed vertical profile (red) to the horizontal beam position (green) as shown in Figure 7 where the alignment correction is marked with the magenta dot. The extrapolation to the beam position suppresses the optics
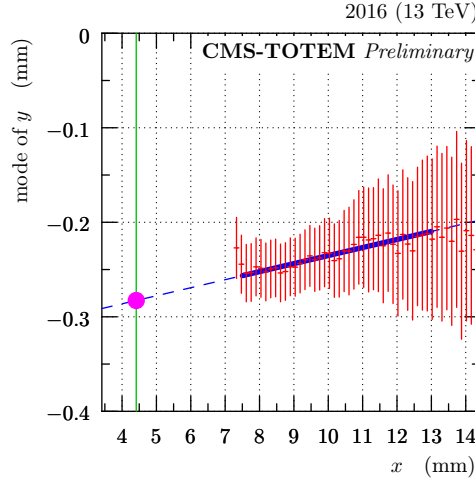
Figure 7: Illustration of vertical alignment (fill 5424, 2016 post-TS2, far RP in sector 45). Red: mode (most frequent value) of y as a function of x, Blue: fit and extrapolation to the horizontal beam position (indicated by the vertical green line and extracted from Figure 6, left). The value of the vertical alignment correction is indicated by the magenta dot. The error bars represent systematic uncertainty.

contributions and keeps the misalignment component only. The mode of y, contrary to the mean of y, is a local estimator not considering the tails of the y distribution which can be truncated e.g. due to the limited sensor size or other acceptance related effects. This vertical alignment method is sufficiently sensitive to provide both absolute per-RP and relative near-far alignment.

Figure 8 shows a summary of per-fill alignment results for one alignment period. It also illustrates one of the many systematic validations performed – compatible results are expected from datasets obtained with different values of the crossing angle, β^*, or different central-detector triggers (the vast majority of the protons reaching the RPs are due to pile up unrelated to the triggering event).

Figure 8 also confirms the expectation of time (or fill) independence of the alignment results. This allows to make a fit of the results to remove occasional outliers, improve fill-to-fill stability and increase the overall accuracy of the alignment. In Run 2, there were two alignment periods where non-negligible time variation was observed for some RPs. A notable example is 2016 pre-TS2 (for details see Section 3.5 in Ref. [26]) where a mechanical package of sensors was initially wrongly inserted in a RP and with time the package slowly drifted to its nominal position thanks to the spring which is included in the RP assembly. Even in these cases, the variation was slow enough that fits could be applied to suppress the excessive fill-to-fill fluctuations and thus improve the results.

A conservative estimate of alignment uncertainties is presented in Table 3. They are estimated from fill-to-fill result fluctuations in cases where identical results are expected.

projection	absolute	relative (near-far)
horizontal	150 μm	10 μm
vertical	100 μm	10 μm

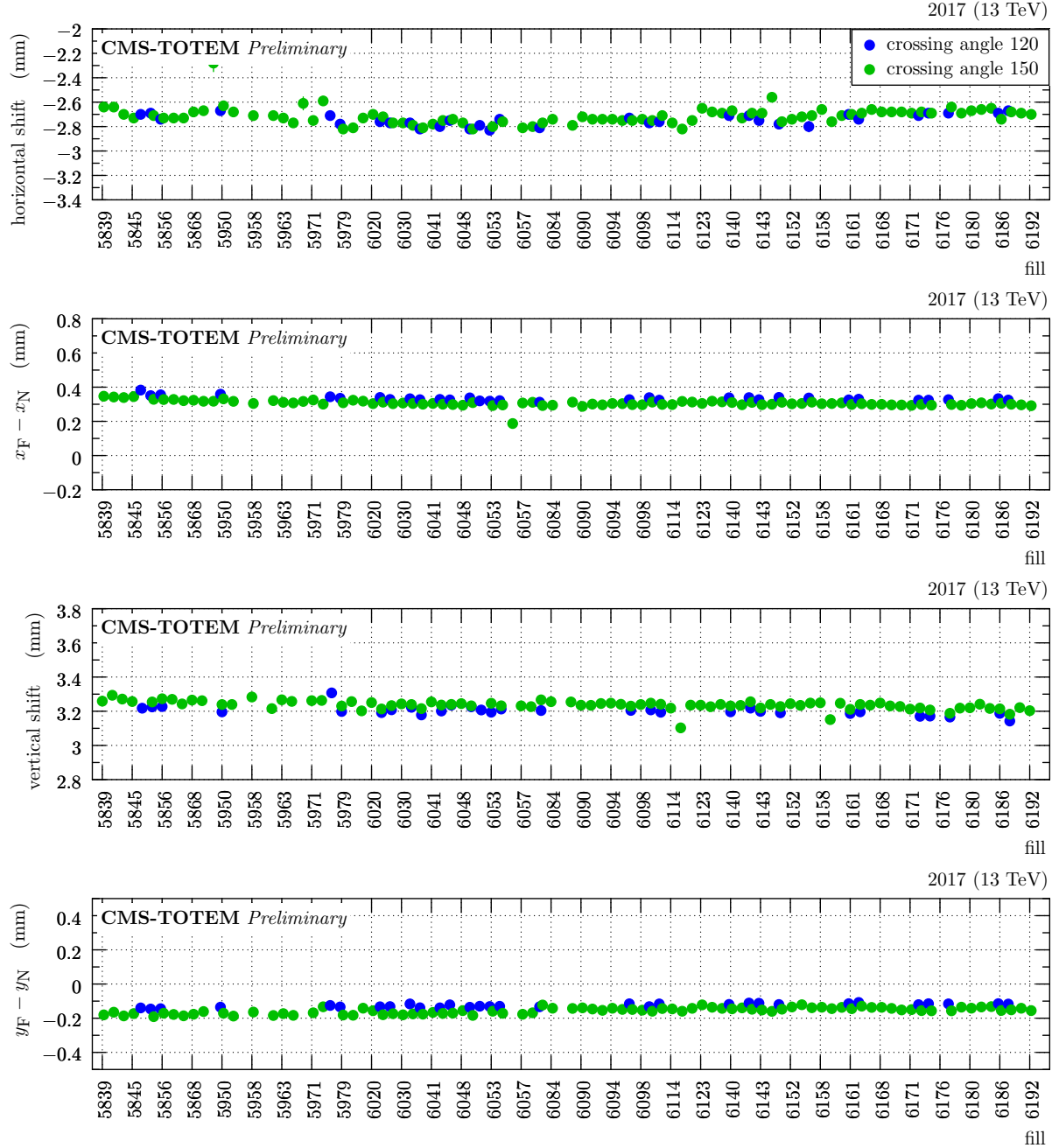Table 3: Summary of per-fill alignment uncertainties.

Figure 8: Example of per-fill alignment results (2017 post-TS2, sector 56 or near RP in sector 56). Horizontal axis represents LHC fills where PPS was active (only some explicitly listed). The colours indicate two values of crossing angle. Rows from top to bottom: absolute horizontal alignment, near-far relative horizontal alignment, absolute vertical alignment and near-far relative vertical alignment.
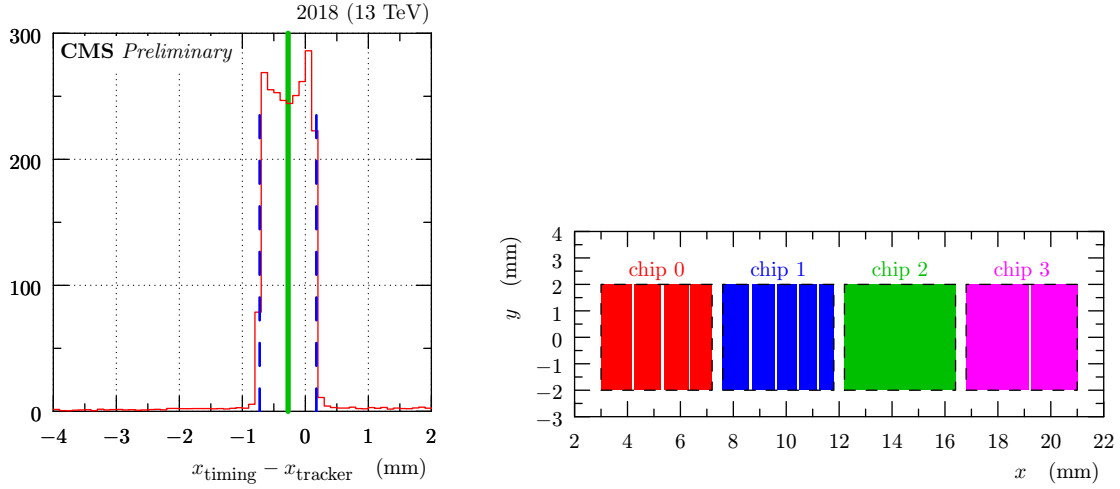
Figure 9: **Left**: illustration of the timing-RP alignment method (fill 7137, 2018, sector 56, plane 1 and pad 9). The red histogram shows the difference between the horizontal track position in the timing sensor, x_{timing}, and the track interpolated from the tracking RPs, x_{tracker}. The vertical blue dashed lines indicate the identified pad boundaries, the green line the pad centre. **Right**: example of timing detector segmentation in one plane (plane 1 in 2018 configuration). The beam would be at $x = 0\,\text{mm}$. Each plane of the timing detectors is composed of four diamond chips, i.e. physical pieces of diamond (represented by a colour, framed by black dashed contours). Each chip may have a different pattern of pads (represented by coloured strips).

5.3 Timing RPs

Timing sensors are aligned with respect to the tracking RPs in order to allow for association of local tracks from timing and tracking RPs, cf. Figure 27. Since the timing RPs have only horizontal segmentation, cf. Figure 9, right, only x alignment is performed. The alignment is performed individually for each plane and pad as well as for each LHC fill.

As illustrated in Figure 9, left, the alignment method is based on a histogram of horizontal differences between the hit position in the timing sensor and the track interpolated from the upstream and downstream tracking RPs. The histogram of these residuals (red) reveals the "shape" of the pad, the pad edges (dashed blue) as well as the pad centre (green). The alignment correction is given by the offset of the green line from zero. A conservative estimate of the uncertainty is $100\,\mu\text{m}$.

A typical example of alignment corrections is shown in Figure 10. As expected, we find compatible results for the pads on the same physical chip, cf. Figure 9, right. The average per-chip correction is indicated by the short horizontal line. The result pattern can be explained by the mechanical process of gluing the chips on the board – the chips cannot mechanically overlap, only additional gaps can be introduced. This leads to a cumulative misalignment monotonously increasing (in absolute value) with the chip number, as revealed by the results. Chip 3, being most far from the beam, often gets no/insufficient track statistics (due to LHC collimators, cf. Section 8) – the correction from chip 2 is used then.
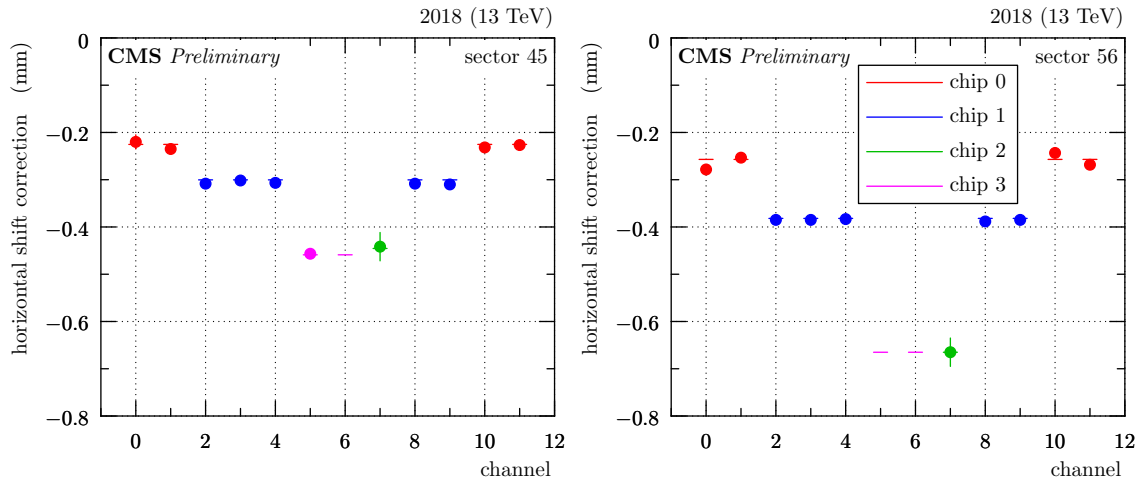
Figure 10: An example of alignment corrections in a single timing-RP sensor plane (fill 7137, 2018, plane 1). Two different markers are used: the dots represent per-channel measurements while the short horizontal lines represent per-chip averages. The same colour is used for channels/pads placed on the same diamond chip, following the scheme in Figure 9, right. For chip 3 (most far from the beam) sometimes the track statistics is insufficient for alignment determination. In such cases the magenta thick dot is missing. **Left**: sector 45, **right**: sector 56.

6 Optics model and calibration

6.1 Introduction

In Run 2, the LHC optics settings and conditions were modified every year. The main concepts and the data-driven tools to constrain the main optical functions for 2016 have been described in Refs. [17, 18]. During physics runs the luminosity of the LHC beams decreases naturally due to bunch intensity decay. Luminosity can be regained for the experiments by increasing the luminosity geometry factor. To achieve this goal in 2017 the levelling of the crossing angle and the betatron amplitude β^* was introduced[1]. In 2018 the levelling of both parameters became continuous [27].

The modelling of this varying optics and its calibration required the generalization of the well-established 2016 methods; the higher statistics permitted, and also required, a more careful dispersion calibration. The vertical position of the beam, y^*, also changed with respect to 2016, and in the last two years of Run 2 the optics had a sizeable vertical dispersion D_y, an important optical function to take into account for the reconstruction. The optics calibration methods of Run 2 are briefly discussed from the viewpoint of the HL-LHC in Ref. [5].

A data driven optics uncertainty model is also presented.

6.1.1 Proton transport at the LHC

The transport matrix and the optical functions have already been introduced in Section 3. In the following, the meaning of the transport matrix elements is explained, with emphasis on the connection between the β amplitude and the optical functions used in the reconstruction. Specifically, the horizontal and vertical magnifications

$$v_{x,y} = \sqrt{\beta_{x,y}/\beta^*} \cos \Delta\mu_{x,y} \tag{7}$$

and the effective lengths

$$L_{x,y} = \sqrt{\beta_{x,y}\beta^*} \sin \Delta\mu_{x,y} \tag{8}$$

are functions of the betatron amplitudes $\beta_{x,y}$, their value β^* at IP5 and the relative phase advance

$$\Delta\mu_{x,y} = \int_{\text{IP}}^{\text{RP}} \frac{\mathrm{d}s}{\beta_{x,y}}, \tag{9}$$

and are particularly relevant for proton kinematics reconstruction.

The beam size can be calculated from the beam emittance ε of the LHC and from the betatron amplitude

$$\sigma(x) = \sqrt{\beta_x \varepsilon} \approx 13 \; \mu\text{m}, \tag{10}$$

where ε is computed from the normalized emittance $\varepsilon_N = (\beta_\text{L} \cdot \gamma_\text{L})\varepsilon = 3.75 \; \mu\text{m}$ rad. Here $\beta_\text{L} = v/c$; v is the velocity of the beam particles, c is the speed of light and $\gamma_\text{L} = (1 - \beta_\text{L}^2)^{-\frac{1}{2}}$ is the Lorentz factor [2]. The Liouville theorem dictates that

$$\pi \cdot \sigma(x) \cdot \sigma(x') = \pi\varepsilon, \tag{11}$$

---

[1]The '*' superscript indicates the LHC IP5

[2]The subscript "L" is used in β_L and γ_L to avoid confusion with the betatron amplitude function β and a γ.

where $\sigma(x')$ is the beam divergence, i.e. the angular smearing, of the LHC beams; the symbol $()'$ stands for d/ds [16]. Therefore, from Eq. (11) it follows that $\sigma(x') = \sqrt{\beta_x^{-1}\varepsilon} \approx 40\ \mu\text{rad}$, which gives the limit on the scattering angle $\theta_{x,y}^*$ resolution of PPS [14].

As already mentioned, in 2017, the necessity to improve the lifetime of the beams led to the change or "levelling" of both the betatron amplitude at IP5 β^* in discrete steps and the horizontal crossing angle. In 2018 both parameters were modified continuously (cf. Table 4). For comparison at IP1 (ATLAS) the crossing angle bump was in the vertical plane during Run 2 in order to avoid long range beam-beam interactions [28]. The levelling is based on the so-called Achromatic Telescopic Squeezing (ATS) optics [27]; one of its features is that the optical functions Eq. (7) and Eq. (8) remain constant despite the change in the β^*. Therefore, the β^* levelling is a transparent operation for viewpoint of the reconstruction. The horizontal dispersion D_x determines the proton trajectory in the horizontal plane and depends on the crossing angle levelling at IP5; therefore D_x is calibrated separately for each reference crossing angle.

Year	Half horizontal crossing angle (mrad)	β^* (m)
2016	140,185	0.4
2017	120,130,140,150	0.3, 0.4
2018	[130, 160]	[0.25, 0.4]

Table 4: Summary of main beam parameter values, crossing angle and β^*, during the Run 2 period per year. In 2017 the values changed in discrete steps, while in 2018 there was a continuous change within the interval.

The transport equation Eq. (1) can be explicitly written at the Roman Pots in the form

$$x = x_0 + x_d(\xi) + L_x(\xi) \cdot \theta_x^* + v_x(\xi) \cdot x^*, \tag{12}$$
$$y = y_0 + y_d(\xi) + L_y(\xi) \cdot \theta_y^* + v_y(\xi) \cdot y^*,$$

which describes the connection between the proton kinematics at the IP5 and at the Roman Pots, where

$$D_x = \frac{x_d(\xi)}{\xi} \tag{13}$$

and D_y are the horizontal and vertical dispersions, respectively, cf. also Ref. [2, 29][3].

The coupling terms m_{ij} in the transport matrix Eq. (5) connect the horizontal and vertical scattering planes. At the LHC, like for most accelerators, these terms are set to zero nominally $m_{13}, ..., m_{42} \approx 0$ for collision optics. They receive perturbative level corrections because of skew quadrupole corrector magnets. The effect of the coupling on the reconstruction of the proton kinematics was found to be negligible for all years.

The optics calibration assumes the beam based alignment of the detectors, after which the beams appear at $x_0 = y_0 = 0$, cf. Eq. (12) [26]. The horizontal position of the protons, $x(\xi)$, is a non-linear function of ξ, which can be approximated for low ξ values

$$x \approx D_x \cdot \xi, \tag{14}$$

where the resolution is limited by the smearing because of the term $\theta_x^* \cdot L_x$; the contribution of the vertex x^* in Eq. (12) is neglected.

---

[3] This formula uses the convention for single pass transport for the dispersion D_x.

6.2 Calibration of the LHC optics

The horizontal dispersion D_x is the most important optics quantity, because it allows to convert the x-coordinate measurements at the Roman Pots into the fractional proton momentum loss ξ. The determination of D_x from the measured proton tracks is briefly reviewed in the next section (cf. also Refs. [17]). The 2017 and 2018 optics calibration procedure goes a step further and also exploits (semi)-exclusive $\mu\mu$ production; the exclusivity of the process plays a key role in the calibration, as illustrated in Section 11.

In the last step the vertical dispersion D_y is determined from minimum bias RP data. The calibration of the dispersion functions is followed by the calibration of the remaining optical functions in the transport matrix Eq. (5), namely the horizontal, $L_x(\xi)$, and vertical, $L_y(\xi)$, effective lengths, and the corresponding magnification functions; other optical functions are less relevant for the proton reconstruction.

The above optics calibration steps rely on the nominal transport model, which is updated from LHC databases. The transport matrix is defined by the machine settings $\mathcal{M}$, which are obtained from several data sources. The proper version of the LHC magnet lattice description, known as sequence, is used each year. The nominal magnet strength file for a given beam optics is always updated using measured data: the currents of the magnet's power converters I_{PC} are first retrieved using TIMBER [30], an application to extract data from heterogeneous databases containing information about the whole LHC infrastructure. The currents I_{PC} are converted to magnet strengths with the LHC Software Architecture (LSA) [31], which uses the conversion curves from the Field Description for the LHC (FIDEL) [32].

6.2.1 The $L_y = 0$ method

This procedure uses the minimum bias data recorded during the special low luminosity runs mentioned in Section 5.1. The method has been applied for each year within Run 2; for 2017 and 2018 a separate calibration was carried out for each crossing angle. The procedure assumes the calibration of the vertical effective length L_y for low-ξ values, below $\xi \approx 4$ % using the elastic candidates measured in the vertical RPs; this additional step is reported in detail in Refs. [17, 33].

The LHC optics is calculated with the Methodical Accelerator Design (MAD-X) program, a general purpose beam optics and lattice software [29]. The vertical effective length $L_y(\xi)$ is a function of the proton momentum loss ξ, and can be calculated with MAD-X at each RP location with good accuracy. The calibration is based on the observation that $L_y(\xi)$ is positive at $\xi = 0$, monotonically decreases with increasing ξ reaching large negative L_y values and it vanishes at about $\xi \approx 4$ %, cf. Figure 11. According to Eq. (12) at this ξ_0 value every proton is transported to the same vertical coordinate $y = 0$ regardless of the vertical scattering angle θ_y^*. At the same time these protons appear at the horizontal location $x_0 \approx D_x \cdot \xi_0$. Consequently, the (x, y) distribution of the protons has to exhibit a "pinch", or focal point, at this horizontal location x_0.

This focal point has been observed and measured with the horizontal RP detectors with large statistics using minimum bias data, as illustrated in Fig. 12. The figure shows the (x, y) distribution of proton coordinates in the RP detectors for 2017 at $\sqrt{s} = 13$ TeV for a representative half crossing angle $\alpha_h = 120$ μrad. The plot shows the parabolic fit of the contour curves around the "pinch" point. The minima of the parabolic curves are fitted with a linear function and the fits are extrapolated. The intersection of the linear fits is marked with a red dot, and indicates the estimate of the focal point position x_0. The fit of the contour lines and the extrapolation are
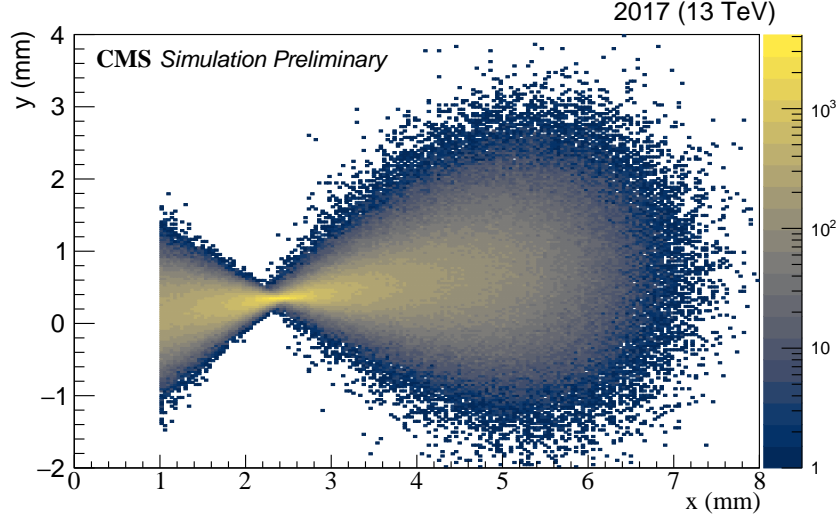
Figure 11: Plot about (x, y) distribution of simulated proton tracks in the near RP in sector 56 using MAD-X. It illustrates the "pinch" or focal point at $x = x_0$ where the vertical effective length vanishes: $L_y(\xi_0) = 0$, given the relation $y \approx L_y(\xi_0) \cdot \theta_y^*$. The simulation takes into account that the small vertical dispersion moves particles upward according to $\Delta y = D_y \cdot \xi$ with increasing x, and ξ.

used in order to estimate the bias coming from the scattering angle terms and extrapolate to zero scattering angle. The measurement is repeated with the distribution obtained after a cut on the scattering angle θ_x to reduce the horizontal smearing around the focal point; in this case the parabolic fits are not needed.

The dispersion is estimated as

$$D_x(\xi)|_{\xi=\xi_0} = \frac{x_0}{\xi_0} . \tag{15}$$

The measured D_x values are used to calibrate the LHC optics model, as described in the next sections.

6.2.2 Calibration using the (semi)-exclusive $\mu\mu$ process

In 2016 PPS collected its first (semi)-exclusive dilepton sample [34]. Section 11 discusses the $\mu\mu$ measurement itself, while here its implications on the optics calibration are presented.

The (semi)-exclusivity implies a high purity data set, where the central $\mu\mu$ system carries the momentum lost by the two forward protons. Therefore, the difference of the fractional momentum loss reconstructed from PPS and from the central CMS detectors can be determined; the correction to D_x is computed such that this difference vanishes. The improved calibration result for D_x remains within the uncertainty of the $L_y = 0$ method and the final D_x result is the weighted average of the two measurements.

The uncertainty of D_x is the combined uncertainty of the $L_y = 0$ and the (semi)-exclusive $\mu\mu$ methods. The evolution of the dispersion $D_x(\xi)$ (or $x_d(\xi)$ cf. Eq. (13)) with ξ can be also validated using the $\mu\mu$ results. The D_x results are shown in Table 5, using a conservative 8 % uncertainty on D_x, which applies to x_d as well.

The dispersion asymmetry between the two arms was observed in 2016 and persisted in 2017 and 2018 as well; it is attributed to crossing angle asymmetry and quadrupole magnet misalig-
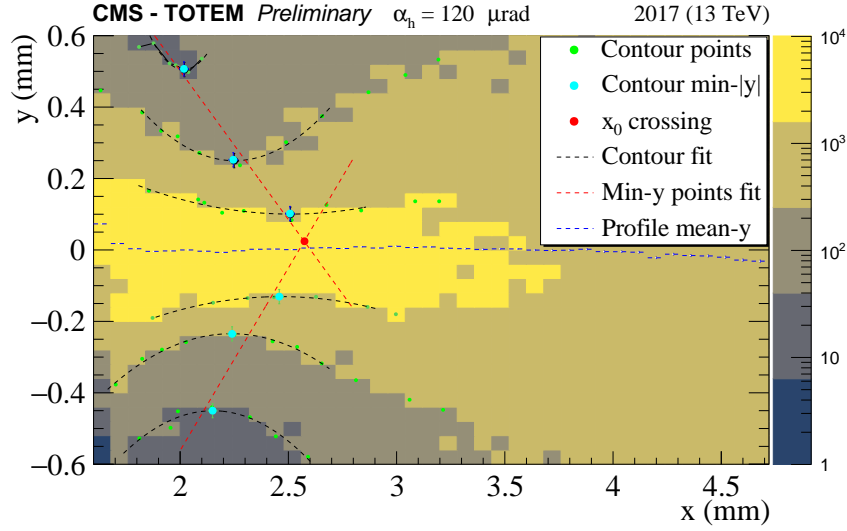
Figure 12: The (x, y) distribution of the proton impact points in the near RP detector in sector 45 for 2017 using minimum bias data is shown, along with parabolic fits of the contours around the "pinch". The minima of the parabolas are fitted with a straight line. The intersection of the two lines is marked with a red dot, and indicates the estimated focal point coordinate x_0. To make the contour curves and extrapolation symmetric, the mean of the histogram was aligned to 0 to remove the y offset created by the vertical dispersion $\Delta y = D_y \cdot \xi$.

ment within their nominal tolerance.

Year	Half crossing angle (rad)	Sector 45 (cm)	Sector 56 (cm)
2016	185	-9.7 ± 0.4	-6.7 ± 0.4
2017	120	-10.4 ± 0.8	-7.9 ± 0.6
2018	120	-11.3 ± 0.9	-8.7 ± 0.7

Table 5: Measured horizontal dispersion values D_x in the near RP at low ξ between 2 % and 4 % (the exact ξ_0 value depends on the detector and the year). The resulting D_x value is the weighted average of the $L_y = 0$ and (semi)-exclusive $\mu\mu$ results. The quoted 8 % uncertainty on D_x applies to the x_d function as well.

6.2.3   Optics matching

The purpose of the optics fitting (or "matching") is the calibration of the LHC optics model using the measured dispersion values and other measured constraints. The calibration procedure consists of a χ^2 minimization with MINUIT, where the initial optics model of the fit is the nominal optics updated from LHC databases, as mentioned in Section 6.2 [35].

The first step is to constrain the quadrupole model using the elastic candidates from the alignment fills, described in Refs. [17]. In the second step the measured dispersion values from Table 5 are used as inputs to the χ^2 function, with additional constraints reflecting the LHC optics uncertainties:

$$\chi^2 = \chi^2_{\text{Design}} + \chi^2_{\text{Measured}} \, . \tag{16}$$

The following measurements from both LHC beams contribute to χ^2_{Measured}:

- the readings of three beam position monitors (BPMs) (at $s = 22$ m, 58 m, 199 m), with an uncertainty $\sigma_{x,absolute} \approx 0.43$ mm ;

- the beam position at RP 210, near, vertical, with an uncertainty $\sigma_x = 0.5$ mm;
- the two measured dispersion values D_x (1 per arm) with their measured uncertainty, cf. Table 5.

In order to match, or fit, the dispersion values and the LHC optics model, the relevant LHC machine parameters are varied during minimization. The matching procedure exploits the fact that a quadrupole magnet misaligned with a δx offset gives a correction to the dipole field, while the quadrupole fields remain unchanged. The following machine parameters have to be matched for the two LHC beams separately to obtain the orbit model for the proton reconstruction:

- Horizontal (half) crossing-angle α_h;
- Quadrupole positions ($\sigma_x = 0.5$ mm, 6 parameters);
- Kicker strength ($\sigma_k \approx 3$ %, 3 parameters).

included into the χ^2_{Design} function [18].

With this procedure a good confidence level was achieved for the lattice model of the two LHC beams. The matched MAD-X optics model is used to extend the measured dispersion values from Table 5 to higher ξ values. An example of the fitted result is shown in Fig. 13.[4]
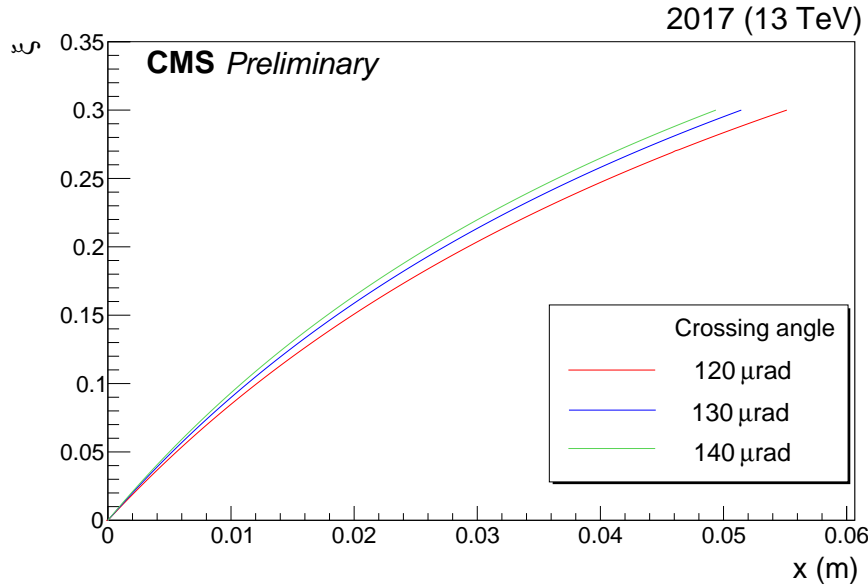

Figure 13: The momentum loss of the protons ξ as a function of x in the near RP of sector 45. The dispersion function is ξ dependent itself and the figure shows directly the obtained non-linear $x(\xi) = D(\xi) \cdot \xi$ function. The $\xi(x)$ function depends on the crossing angle as well; the figure shows the dependence for three reference angles, which permits to interpolate the function to arbitrary intermediate angles.

The optics model MAD-X shows that the different interpretations of the dispersion asymmetry (crossing angle rotation, quadrupole misalignment, etc.) lead to negligible differences in the systematic uncertainty, for example in the evolution of D_x with ξ.

---

[4]This matching procedure has been reviewed by the beam department (BE) experts of the LHC.

6.2.4 Calibration of the vertical dispersion D_y

In 2016 the vertical dispersion D_y was close to zero, while in 2017 and 2018 the optics changed and a vertical dispersion $D_y \approx -1$ cm was applied. Despite its small value, the vertical dispersion has a strong effect on the ζ dependence of the vertical reconstruction of θ_y^* and y^* because of the non-linearity of the other optical functions, cf. Fig. 14.

The vertical dispersion D_y is calibrated by perturbing its value in the near and far RP, so as to obtain two linear equations for the corresponding changes both in θ_y^* and y^* measured at a given ζ value. The simple linear equation system can be solved by inverting the coefficient, or derivative, matrix ΔJ in order to compute the corrections to the vertical dispersion.
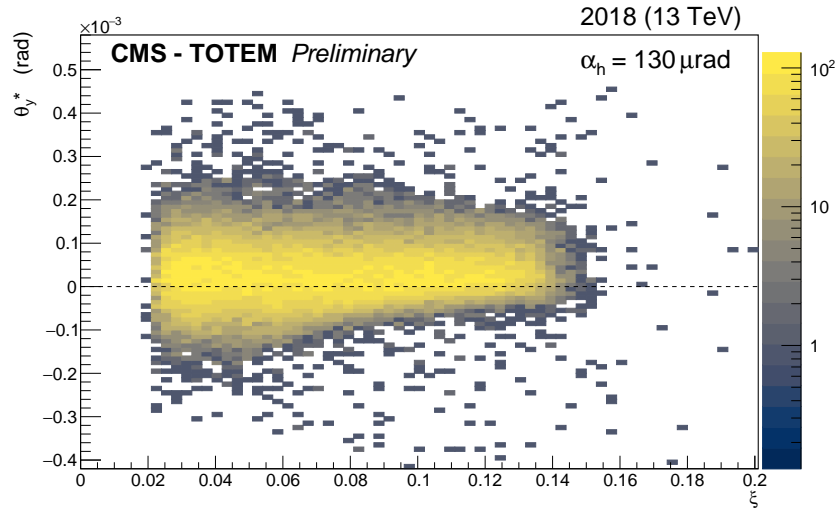

Figure 14: The plot shows the vertical scattering angle θ_y^* as a function of ζ after calibration of the vertical dispersion D_y for sector 45 and fill 6923. The mean of the scattering angle distribution is well aligned to 0. The distribution is also affected by the vertical acceptance limitations starting from about $\zeta \approx 5$ % due to the vertical acceptance limits of the detector cf. Fig. 3.

The measured vertical dispersion values are summarized in Table 6. The values are small enough that the crossing angle dependence can be neglected. The vertical dispersion values D_y are validated with minimum bias data, cf. Section 7 and also Fig. 14.

Year	Sector 45 (cm)	Sector 56 (cm)
2016	0 ± 0.02 (statistical)	0 ± 0.02 (statistical)
2017	-1.36 ± 0.02 (statistical) ± 0.1 (systematic)	-1.99 ± 0.02 (statistical) ± 0.16 (systematic)
2018	-1.36 ± 0.02 (statistical) ± 0.1 (systematic)	-1.87 ± 0.02 (statistical) ± 0.15 (systematic)

Table 6: Final measured vertical dispersion values D_y in the near RP per year. The result is derived using the horizontal dispersion D_x included into the systematic uncertainty.

6.3 Optics description and uncertainty model

The LHC optics model, calculated with MAD-X, can be described in several efficient ways for the reconstruction and physics analysis [29]. In the year 2016 the description of the proton transport used orthonormal polynomials to fit the (x, y) coordinates of the protons at the RPs as a function of their input kinematics [36].

Experience with the data and optics modelling showed that the parametrization, or factorization, Eq. (12) is sufficient to describe the proton transport between IP5 and the RPs, thus since 2016 an expansion using only 1-dimensional ξ dependent optical functions is applied.
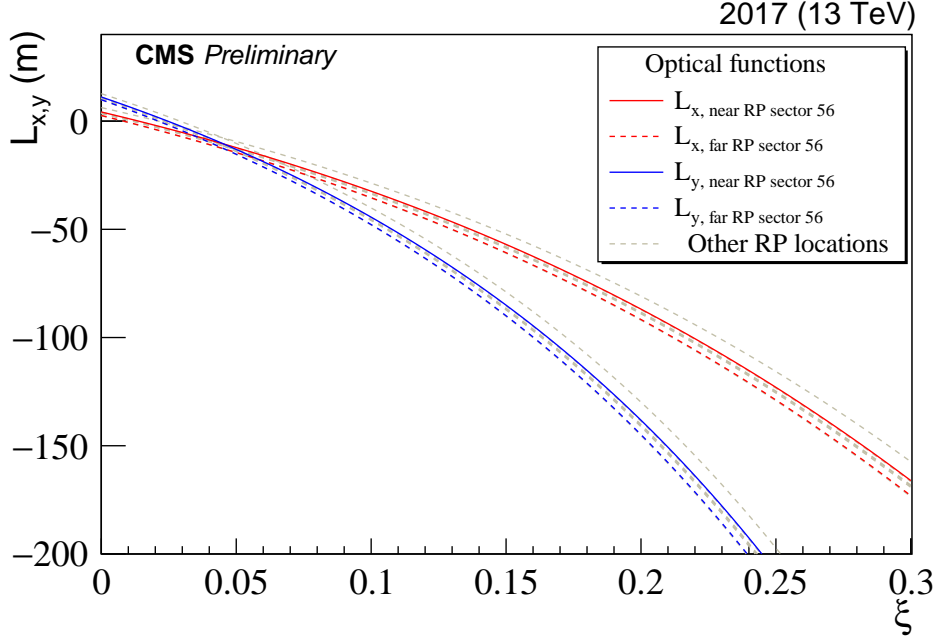

Figure 15: The horizontal and vertical effective lengths L_x and L_y transport the scattering angle of the proton at IP5 θ_x^* and θ_y^* to the position (x, y) at the Roman Pots. The figure shows the ξ dependence of the two functions. The horizontal effective length $L_x(\xi)$ decreases faster than the vertical function L_y; both of them cross zero at low ξ, below $\xi = 5\,\%$. The grey dashed lines show the TOTEM RPs used only for calibration.

As discussed earlier, in 2017 the levelling of the beam crossing angle was introduced. This is straightforward to take into account using the optical function concept with an additional interior extrapolation function among reference crossing-angles, as shown in Eq. (17) and Fig. 13:

$$x(\alpha_h, \xi) = x_{120}(\xi) + \frac{120 - \alpha_h}{120 - 140} \cdot [x_{140}(\xi) - x_{120}(\xi)] . \tag{17}$$

The linear function is motivated by MAD-X and is compatible with the dispersion measurements within uncertainty. The other optical functions remain constant during the levelling of the crossing angle and, thanks to the telescopic concept of the ATS optics, they also remain constant during the levelling of the β^*. The relevance of the ATS telescopic squeezing from the viewpoint of uncertainty model is discussed in Section 6.3.1.

6.3.1 Optics uncertainty model

The uncertainties of the horizontal and vertical dispersions D_x and D_y, and of the function $x_d(\xi)$ have already been discussed in Section 6.2 and 6.2.4 (cf. also Table 5). The uncertainties of the remaining relevant optical functions are illustrated in the following.

The levelling of the crossing-angle and β^*, mentioned earlier, is based on the ATS optics, which has been conceived to cope with requirements expected for HL-LHC [27]. The most important feature of the ATS optics, from the viewpoint of the forward spectrometers, is that the magnetic fields around the IP are kept stable during the levelling process. The β^* at these IPs is changed by varying magnets at IP2 and IP8 [27]. This stability significantly reduces the uncertainty on

the optics model and transport matrix for PPS. It also contributes to the alignment stability, which uses the distribution of $\frac{L_y}{dL_y/ds}$, cf. Eq. (6) and Eq. (12).

Despite its stability, the real LHC machine [37] is subject to additional imperfections $\Delta\mathcal{M}$, which alter the transport matrix by ΔT:

$$T\left(s;\mathcal{M}\right) \to T\left(s;\mathcal{M}+\Delta\mathcal{M}\right) = T\left(s;\mathcal{M}\right)+\Delta T. \tag{18}$$

The principles of the optics uncertainty model are described in Refs. [17]. A more complex approach is however needed in view of the explicit ξ dependence of the optical functions.

The transport of protons in the vicinity of the central orbit, or any other reference orbit with a certain ξ, is mainly determined by the quadrupole fields of the alternating focusing and defocusing magnet (FODO) system of the LHC, while the position of the central orbit itself is determined by the distribution of the dipole fields; this includes the dipole fields created by misaligned quadrupole magnets.
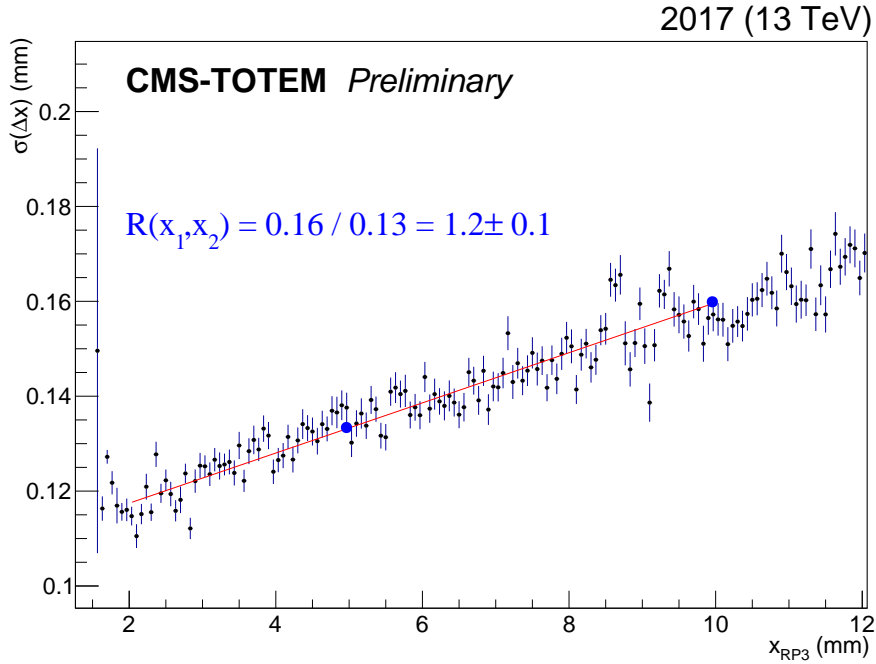

Figure 16: Fit of $\sigma(\Delta x)$ as a function of x for the near RP in sector 45. The fit is used to esimate the uncertainty of the optical function dL_x/ds.

A typical example is the assessment of the uncertainty of the optical function dL_x/ds. The estimation starts with the uncertainty model at low ξ; the magnets' strengths k in MAD-X are perturbed within their nominal uncertainty and the model is refined using the optics constraints from elastic candidates. In the next step the ratio of the optical function is estimated between the low- and high-ξ part using data driven methods, cf. Fig. 16. The estimation is based on the relation $\Delta x(x_1) = \left. dL_x/ds\right|_{x=x_1} \cdot \theta_x^*$ and exploits the fact that the scattering angle distribution of the proton is almost independent of ξ, so that

$$R(x_1, x_2) = \frac{\sigma(\Delta x(x_2))}{\sigma(\Delta x(x_1))} \approx \frac{\left. dL_x/ds\right|_{x=x_2}}{\left. dL_x/ds\right|_{x=x_1}}. \tag{19}$$

After careful evaluation for this particular function the optics model and the data agree within $\approx 10\,\%$, cf. Fig. 16. The $R(x_1, x_2)$ result is translated to $R(\xi_1, \xi_2)$ using the dispersion and, together with the low-ξ uncertainty, determines the uncertainty at all ξ. A similar procedure leads to the uncertainty of $L_y(\xi)$. The LHC optics gives strict correlations between the magnifications v_x, v_y and L_x, L_y. Therefore, the uncertainty estimation of the effective lengths indirectly provides uncertainties on the magnifications as well.

6.3.2 Covariances of optical functions

In order to fully estimate the ξ dependence of the uncertainty of the optical functions, the calculation of the covariance matrix between different ξ values for each function is needed. The magnetic strength k and other relevant beam parameters are perturbed within their nominal uncertainty and the optical functions are calculated for each parameter set. The values of the obtained optical functions L_x and the envelope function thus obtained are shown in Fig. 17. The covariance and correlation matrix for the optical function L_x at the fractional proton momentum loss $|\xi| = 3\,\%$ and $|\xi| = 10\,\%$ are shown in Table 7.
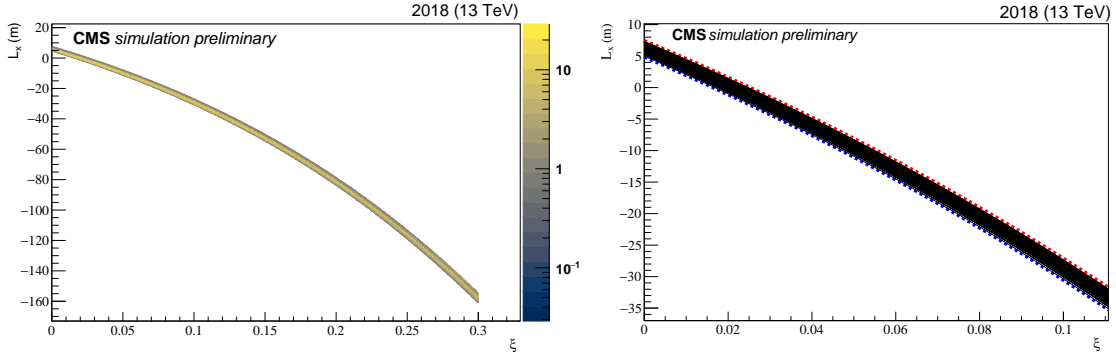

Figure 17: Left: the distribution of the horizontal effective length $L_x(\xi)$ values as a consequence of perturbations of the magnetic strength. Right: graph to show the correlations of the functions; the red and blue dashed curves represent the two extreme $L_x(\xi)$-curves of the Monte Carlo. They are the upper and lower envelope, thus they demonstrate that the points of the curve move together at different ξ.

The correlation matrix, shown in Table 7, indicates a close to 100\,% correlation between the low- and high-ξ, which is taken into account in the uncertainty model, cf. also Fig. 17. This means that the variation of the magnetic strength and other beam parameters act in the same way at different ξ values and the uncertainty can be described with one parameter. The covariance and correlation matrices are available for all optical functions.

	$|\xi| = 3\,\%$	$|\xi| = 10\,\%$
3\,%	1.0	0.996
10\,%	0.996	1.0

Table 7: The correlation matrix for L_x between different ξ values for the detector RP56-220-fr vertical.

The optics uncertainty model takes into account the close to 100\,% correlation. This means that the optical function perturbation δo can be determined at a given reference ξ_{ref} value and can then be scaled with the factor given in Fig. 18 to obtain the perturbation at a different ξ value. The optics uncertainty model is included in the PPS proton simulation described in Section 9.
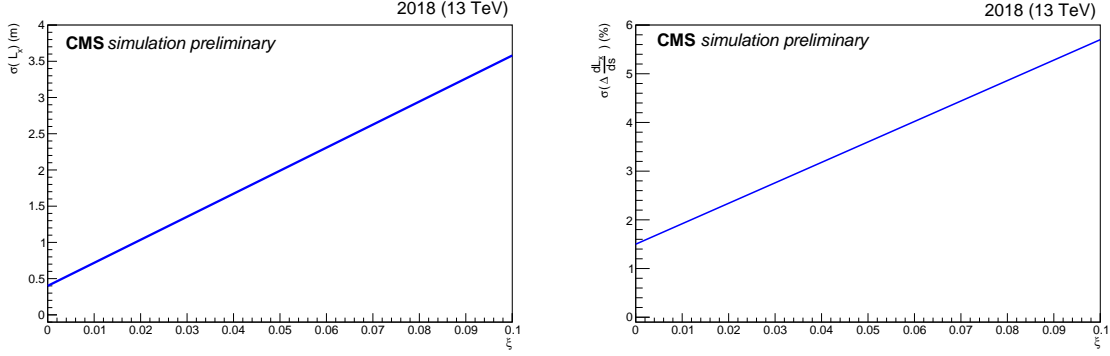
Figure 18: Left: ξ dependent uncertainty function of the horizontal effective length $L_x(\xi)$. Right: ξ dependent uncertainty function of the derivative of the horizontal effective length $\mathrm{d}L_x(\xi)/\mathrm{d}s$.

6.3.3 Inversion of the proton transport equations

The transport equations Eq. (12) are linear in ξ and in the horizontal scattering angle θ_x^*, with coefficient functions like $L_x(\xi)$ which are non-linear. The beam size $\sigma(x)$ from Eq. (10) multiplied by the magnification factor $|v_x| \approx 4$ gives $\sigma(x) \cdot v_x \approx 60~\mu$m in the horizontal plane, a contribution which is negligible when compared to the other two terms. Therefore, the equation system Eq. (12) can be inverted to yield:

$$\xi = \frac{L_{x,\mathrm{far}} \cdot x_{\mathrm{near}} - L_{x,\mathrm{near}} \cdot x_{\mathrm{far}}}{D_{x,\mathrm{eff,near}} \cdot L_{x,\mathrm{far}} - D_{x,\mathrm{eff,far}} \cdot L_{x,\mathrm{near}}} \,, \quad \theta_x^* = \frac{1}{\mathrm{d}L_x/\mathrm{d}s} \left(\theta_x - \frac{\mathrm{d}D_x}{\mathrm{d}s} \xi \right) , \tag{20}$$

where the optical functions, like $L_{x,\mathrm{near}}(\xi)$, are functions of ξ. The variable ξ appears on both sides of the first non-linear equation, whose solution can be found with any iterative method. The obtained formulae are similar to those developed and used previously by the TOTEM collaboration [25]. Equation (20) indicate the optical functions whose calibration is most relevant for the reconstruction. The formulae for the vertical reconstruction

$$y^* = \frac{L_{y,\mathrm{far}} \cdot y'_{\mathrm{near}} - L_{y,\mathrm{near}} \cdot y'_{\mathrm{far}}}{v_{y,\mathrm{near}} \cdot L_{y,\mathrm{far}} - v_{y,\mathrm{far}} \cdot L_{y,\mathrm{near}}} \,, \quad \theta_y^* = \frac{1}{\mathrm{d}L_y/\mathrm{d}s} \left(\theta_y - \frac{\mathrm{d}v_y}{\mathrm{d}s} y^* \right) , \tag{21}$$

where $y' = y - D_y \cdot \xi$. The non-linear equation Eq. (21) shows that an otherwise constant offset in D_y, or in the vertical alignment would lead to a non-linear distortion of the reconstructed angle.

In summary, the LHC optics settings and conditions changed every year in Run 2. In this chapter the main concepts and the data-driven tools to constrain the optical functions for 2016, 2017 and 2018 have been presented. The main challenges of Run 2 are the levelling of the instantaneous luminosity by changing the crossing angle and β^*, which requires the careful calibration of the horizontal dispersion D_x and also its change with the crossing angle. The vertical dispersion D_y became sizeable in 2017 and 2018, its calibration has been discussed. An optics uncertainty model has also been presented, which includes the covariance matrix of transport elements.

7 Proton reconstruction

The proton reconstruction consists in back-propagating the protons from the RPs (where they are measured) to the IP (where the kinematics is determined). The propagation follows the LHC optics discussed in Section 6. The input to the propagation consists of the proton tracks detected by the RPs and aligned with respect to the LHC beam (cf. Section 5). Since the proton tracks at the RPs are linear (no magnetic field), they can be described by four independent parameters (slopes and intercepts along x and y). The proton kinematic variables include: the transverse position of the proton at $z = 0$, x^* and y^*, the horizontal and vertical scattering angles, θ_x^* and θ_y^*, and the fractional momentum loss, ξ – that is five parameters. Compared to the four parameters measurable by the RPs, in general, the reconstruction problem is under-constrained and a variable must be fixed with external information. Two complementary reconstruction strategies are exploited: single-RP and multi-RP.

The **single-RP** reconstruction is a simple approach that uses information from single RPs only. Because of the reduced input information, only ξ and θ_y^* can be estimated:

$$\xi = x_{\mathrm{d}}^{-1}(x) \, , \qquad \theta_y^* = \frac{y}{L_y(\xi)} \, , \tag{22}$$

where ξ reconstructed from the former equation is inserted to the latter. These equations reflect only the leading terms from the optics decomposition in Eq. (12). Neglecting the sub-leading, but still relevant, terms (e.g. the one proportional to θ_x^*) implies a degraded resolution. On the other hand, a notable advantage of this approach is its applicability even when the proton track is not available in the other RP(s) of the arm. Furthermore, this approach has a different (slightly smaller) dependence on the systematic perturbations with respect to multi-RP method, cf. Figure 37. In this sense the single-RP reconstruction is a very useful check of the calibration. The variables x^*, y^* and θ_x^* cannot be reconstructed with this approach and they are set to zero. For the vertex coordinates this is a reasonable approximation when low β^* optics is used (as detailed below).

The **multi-RP** reconstruction aims at exploiting the full potential of the spectrometer: it searches for proton kinematics that matches best the observations from all RPs and all projections by minimising the following function:

$$\chi^2 = \sum_{i:\,\mathrm{RPs}} \sum_{q:\,x,y} \left[\frac{d_q^i - (T^i d^*)_q}{\sigma_q^i} \right]^2 \, , \tag{23}$$

where i runs over all the tracking RPs in the arm and q over the two transverse projections. This expression follows the notation of Eq. (1): the vector d^i represents the (measured) proton position at the i-th RP, the vector d^* denotes the proton kinematics at the IP and the matrix T^i stands for the proton transport between the IP and the i-th RP. The quantity σ_q^i denotes the position measurement uncertainty at the i-th RP in projection q. This general formulation allows for using any optics model, T, and any number of tracking RPs (greater than 1). A similar approach proved useful already when applied by the TOTEM Collaboration to high β^* optics [36]. Since PPS aims primarily at low β^* optics, further optimisations are possible. Low β^* optics is characterised by narrow distributions of interaction vertices in the transverse plane, $\sigma(x^*) \approx \sigma(y^*) = \mathcal{O}(10\,\mu\mathrm{m})$. Consequently, the vertex terms in the optics decomposition of Eq. (12) give only a small contribution and can be neglected in the reconstruction without any significant loss of accuracy (cf. Figure 35, right). This, in turn, can resolve the under-determinacy of the reconstruction discussed earlier. Since there are only 4 measurements available (2 projections times 2 RPs), only 4 proton parameters out of total five (x^*, y^*,

θ_x^*, θ_y^*, ξ) can be determined. Therefore, by default, in reconstruction x^* is fixed to 0 which is a reasonable approximation given the LHC optics used by PPS (low $\beta*$) and very small x^* RMS in these conditions. In this case the number of degrees of freedom for the fit is ndf $= 4 - 4 = 0$ and therefore the fit effectively performs a numerical solution of a set of 4 non-linear equations. It is equally justified to fix also $y^* \equiv 0$, which results in an alternative fitting model with one less fitted parameter (since ξ is reconstructed from horizontal coordinates) and thus with ndf $= 4 - 3 = 1$. This option has been tried for validation purposes and yields results compatible with those obtained with the default choice.

The general expression in Eq. (23) can be decomposed into a set of simpler equations for the conditions relevant to PPS. If two tracking RPs are used per arm (Run 2 configuration), if the proton transport can be approximated by the terms explicitly mentioned in Eq. (12) (very good approximation for 2017 and 2018) and if only x^* is assumed to be zero (the case with ndf $= 0$), then the minimum of χ^2 from Eq. (23) is described by Eqs. (20) and (21). Each of these equations gives an explicit expression to determine one of the proton kinematic variables. Only the first equation is non-linear (ξ on both sides of the equation), while the others are linear (ξ is taken from the solution to the first equation). Beyond the usefulness for optics studies as discussed in Section 6, this decomposition can speed up the reconstruction software implementation: there is a single non-linear equation with a single variable which can be solved in different well known ways, e.g. the Newton method. Using this optimisation gives results compatible with the full minimisation according to Eq. (23).

During Run 2, PPS was operated with two tracking RPs per arm (denoted "near" and "far", referring to their position with respect to the IP). The input to Eq. (23) therefore consists of one near and one far RP track, selected such that their combination is consistent with belonging to a proton originating from the IP. The selection is achieved by considering all near-far track combinations and retaining only those fulfilling the so called "near-far association" cuts. This selection has a double aim: first, to suppress background, and second, to disentangle multiple forward protons present in the event. The association cuts reflect the expected proton kinematics at the IP (e.g. the RMS of the scattering angles) and the patterns imposed by the LHC optics. For instance, forward protons arrive to the RP detectors at small angles with respect to the LHC beam and therefore Δx and Δy are expected to be small, of the order of 0.1 mm (Δ refers to the near-far difference of the track position). Beyond these, selection criteria based on $\Delta\xi$ and $\Delta\theta_y^*$ are also used, based on the single-RP reconstruction of Eq. (22). The cuts have been tuned using both MC simulation and data, with the aim of optimising for efficiency and purity. The inefficiency (further discussed in Section 12) can arise either because of overly strict cuts discarding real protons, or overly loose cuts not able to distinguish between two (or multiple) protons in the event. The optimisation of the near-far association cuts is performed for each year. In 2016 and 2017, some of the RPs were equipped with Si strip sensors allowing to reconstruct no more than one track per event. In this case, the association cuts can only suppress background and can thus be relatively loose: typically only the $\Delta\xi$ criterion with threshold of about 0.01 is applied. In 2018, all tracking RPs were equipped with Si pixel sensors capable of reconstructing multiple tracks. Disentangling individual protons becomes necessary and tighter cuts are then needed: typically $\Delta\xi$ (threshold of about 0.008), Δy and $\Delta\theta_y^*$ criteria are applied.

The quality of the multi-RP reconstruction can be benchmarked by re-propagating the reconstructed protons to the RPs and comparing the positions of the measured and the re-propagated track impact points – the typical difference is smaller than 1 μm (thus at least an order of magnitude better than spatial resolution of the RPs).

Figure 19 compares the results of the single-RP reconstruction of ξ from the near and far RPs.
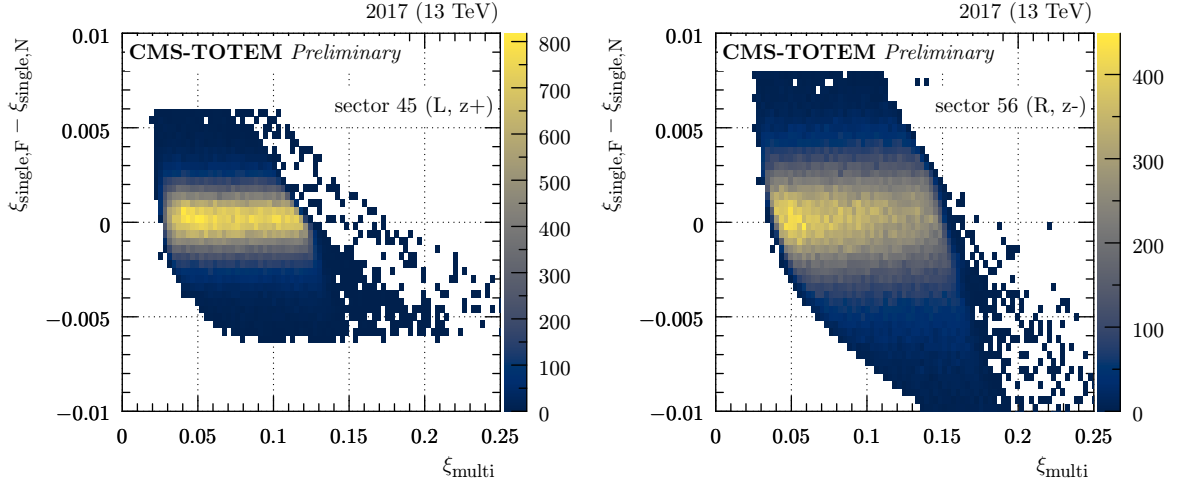
Figure 19: Comparison of ξ reconstructed with the single-RP method from the near and far RP in each arm, presented as a function of ξ (fill 5849, 2017). **Left**: sector 45, **right**: sector 56.

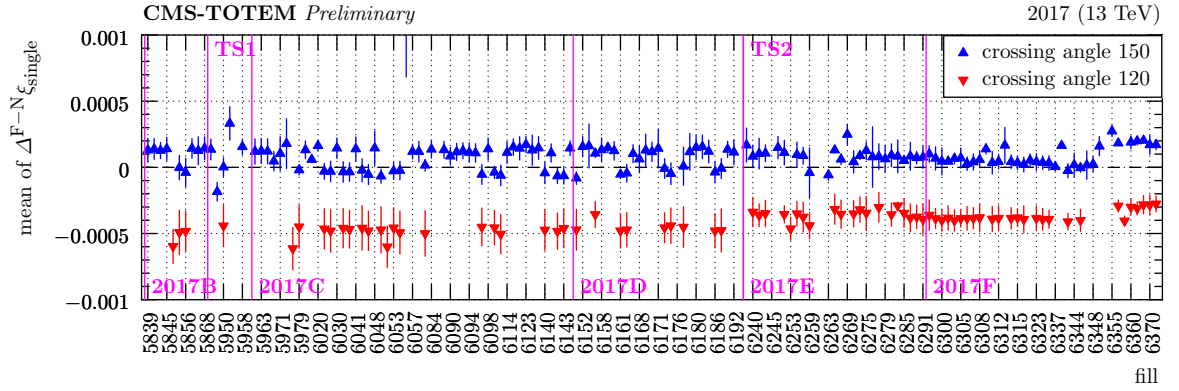Figure 20: Mean near-far ξ difference from single-RP reconstruction (in a safe region far from acceptance limitations) as a function of fill (2017, sector 56). The different colours represent data taken with different values of the crossing-angle. The error bars represent a systematic uncertainty estimated as a difference of means evaluated at two different values of ξ_{multi}.

The observed part of the phase space (reflected by the discontinuities in the plots) is limited by the distances of the RPs from the beam (at low ξ_{multi}) and LHC aperture limitations (at high ξ_{multi}, details given in Section 8). Beyond these acceptance limitations, the difference is distributed symmetrically about 0 and is independent of the reconstructed ξ (multi-RP), as expected if the alignment and the optics calibration are correct. An example summary of the mean difference for multiple fills is presented in Figure 20. The mean is stable in time, as expected. The systematic shift between the blue and red markers (different values of crossing-angle) can be attributed to a residual mis-calibration and represents a measure of the systematic uncertainty of the reconstruction.

Figure 21 shows a comparison of ξ reconstructed with the single-RP and the multi-RP methods. Within resolution, they are expected to give the same results. As expected the single-RP reconstruction has a rather low resolution (a quantification is available e.g. in Figure 39). Apart from acceptance limitations (cf. Section 8), the single-multi difference is symmetrically distributed about 0 and has a mean independent of ξ, again as expected if the alignment and the optics calibration are correct. A summary of the mean single-multi ξ difference for several fills is shown in Figure 22. The mean is stable with time and close to zero (within the estimated uncertainties,
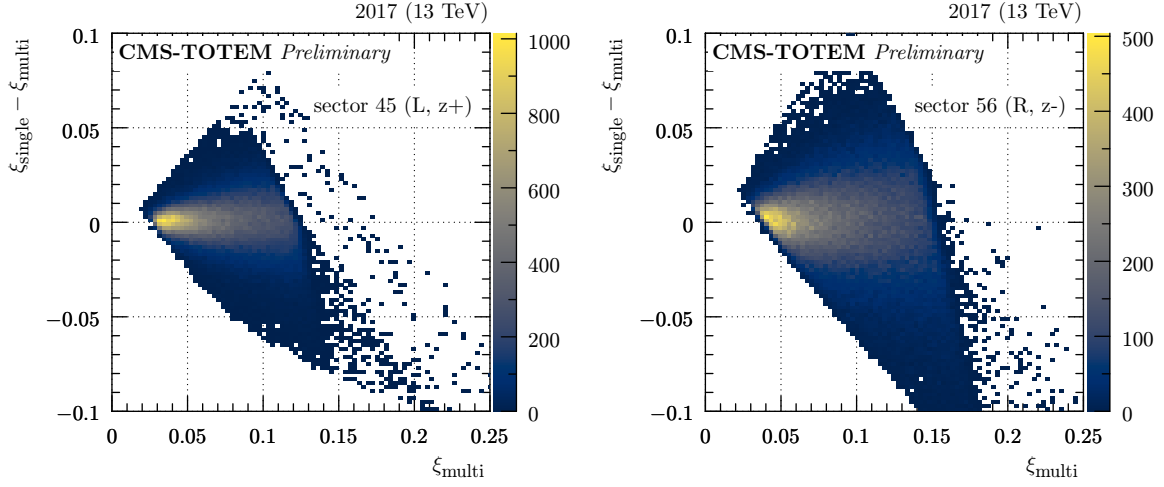
Figure 21: Comparison of ξ reconstructed with the single-RP and multi-RP methods, presented as a function of ξ (LHC fill 5849, 2017, single-RP reconstruction from the near RPs). **Left**: sector 45, **right**: sector 56.
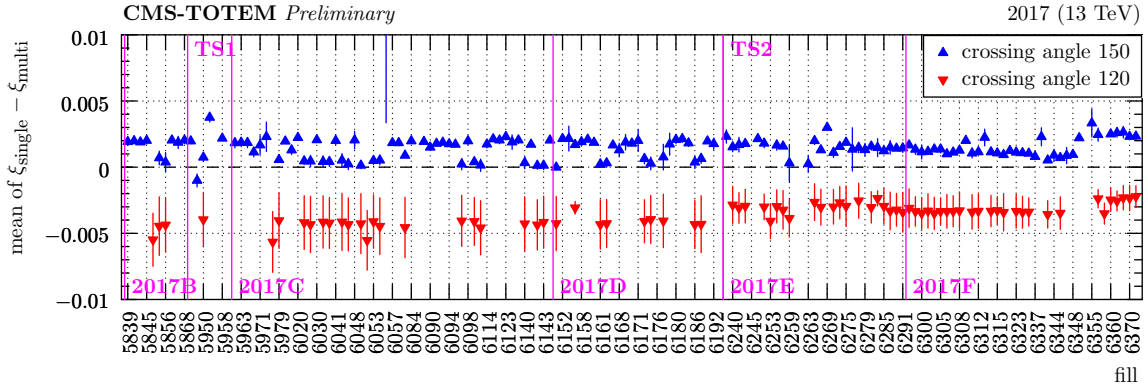

Figure 22: Mean single-RP vs. multi-RP ξ difference (in a safe region far from acceptance limitations) as a function of fill (2017, sector 56, single-RP reconstruction from the near RP). The different colours represent data taken with different values of the crossing-angle. The error bars represent a systematic uncertainty estimated as a difference of means evaluated at two different values of ξ_{multi}.

Figure 39). There is a small residual dependence on the crossing-angle (colours), which is due to residual mis-calibration and represents a contribution to the systematic uncertainties.

Figure 23 shows an example distribution of the horizontal scattering angle, θ_x^*, vs. ξ as reconstructed with the multi-RP method. The θ_x^* distribution is expected to be symmetric about zero. Apart from acceptance limitations (cuts at white-blue boundaries) we observe a result compatible with this expectation. Specifically, the mean value of θ_x^* does not depend on ξ – a requirement for well calibrated conditions. Figure 24 compares mean θ_x^* from several fills. The mean is stable over time and close to zero (within approximately $\pm 10\,\mu\mathrm{rad}$). The small residual dependence on the crossing-angle (colours) is again taken as a systematic uncertainty of the reconstruction.

Figure 25 shows an example distribution of the vertical scattering angle, θ_y^*, vs. ξ as reconstructed with the multi-RP method. The θ_y^* distribution is expected to be symmetric about zero. Besides the low-ξ region in the left plot (sector 45) which is affected by radiation damage
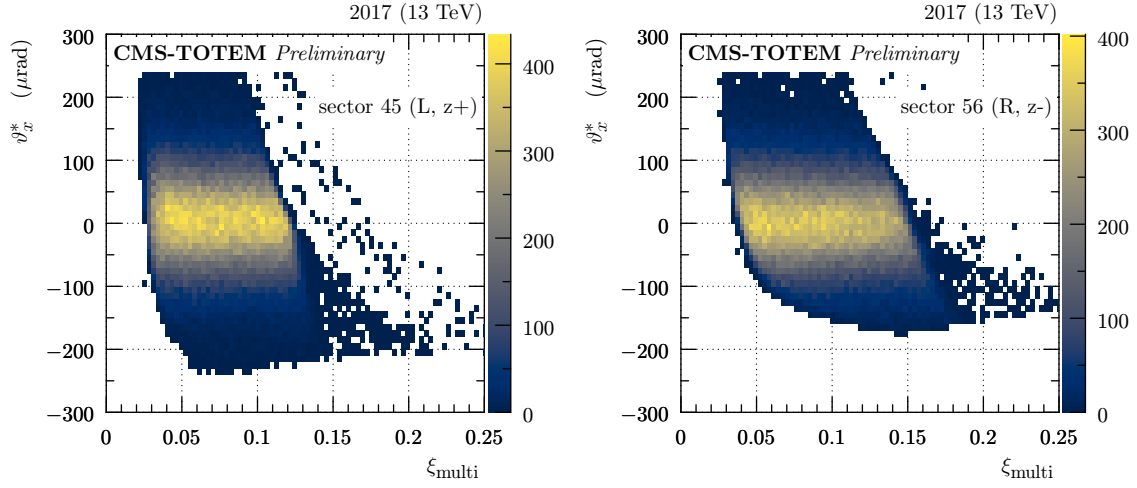
Figure 23: Histogram of θ_x^* vs. ξ as reconstructed with the multi-RP method (fill 5849, 2017). **Left**: sector 45, **right**: sector 56.
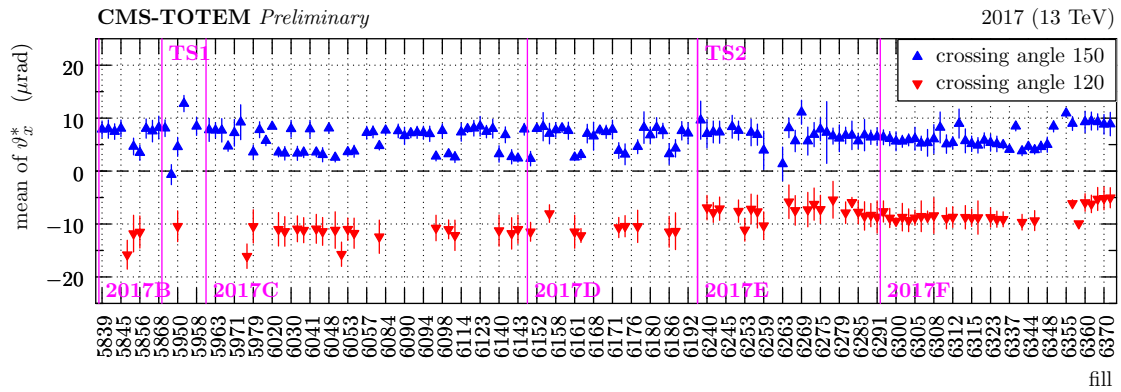

Figure 24: Mean value of θ_x^* (in a safe region far from acceptance limitations) as a function of fill (2017, sector 56). The markers in different colours represent data taken with different values of the crossing-angle. The error bars represent a systematic uncertainty estimated as a difference of means evaluated at two different values of ξ_{multi}.
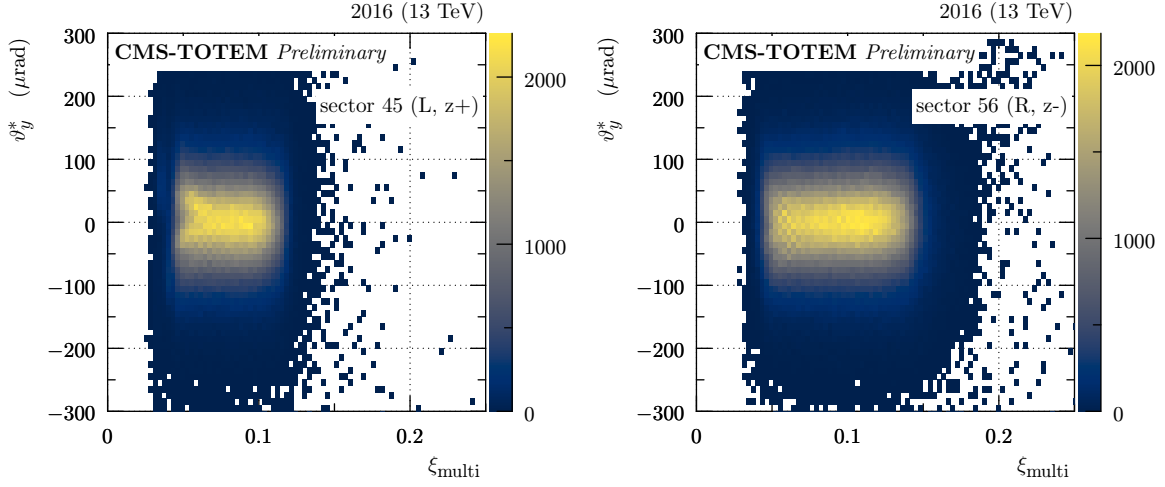
Figure 25: Histogram of θ_y^* vs. ξ as reconstructed with the multi-RP method (fill 5276, 2016). **Left**: sector 45, **right**: sector 56.
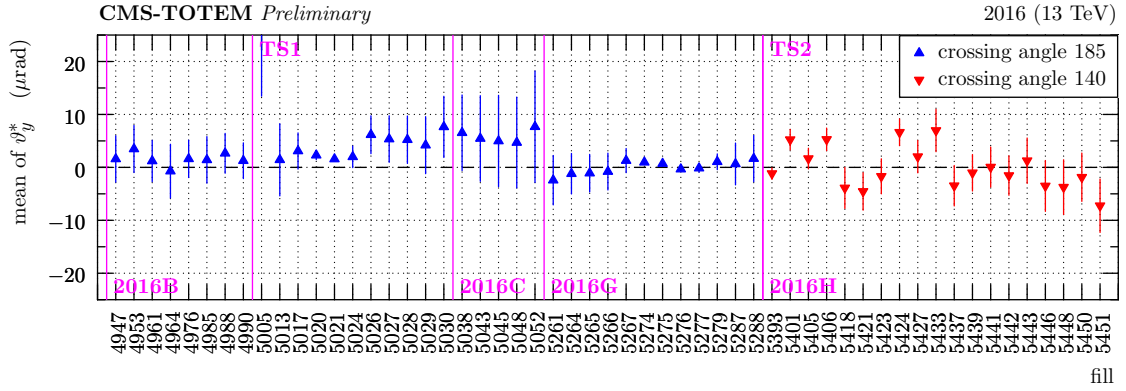

Figure 26: Mean value of θ_y^* (in a safe region far from acceptance limitations) as a function of fill (2016, sector 45). The markers in different colours represent data taken with different values of the crossing-angle. The error bars represent a systematic uncertainty estimated as a difference of means evaluated at two different values of ξ_{multi}.

(cf. Section 12), we find this symmetry well fulfilled. A collection of θ_y^* mean values extracted from several fills is presented in Figure 26. The mean is stable over time and close to zero (within $\pm 10\,\mu$rad). Note that only a single value of the crossing angle was used in each of the pre- and post-TS2 periods in 2016, these values were mutually different in the two periods.

The reconstructed proton objects provided for physics analyses combine:

- proton kinematics at the IP: deduced from tracking RP measurements (as discussed above) and
- proton timing information: determined from timing RPs.

The timing information can be used to match PPS protons with a vertex in the central detector and thus for background suppression, cf. Section 13.

Tracks from the tracking and timing RPs are matched based on Δx, the difference between the x coordinate measured in the timing RP and that interpolated from the tracking RPs, cf. Figure 27. The shape of the histograms effectively reveals the "shape" of the timing pad, somewhat smeared by the limited resolution. The tracking and timing tracks are matched if the ratio
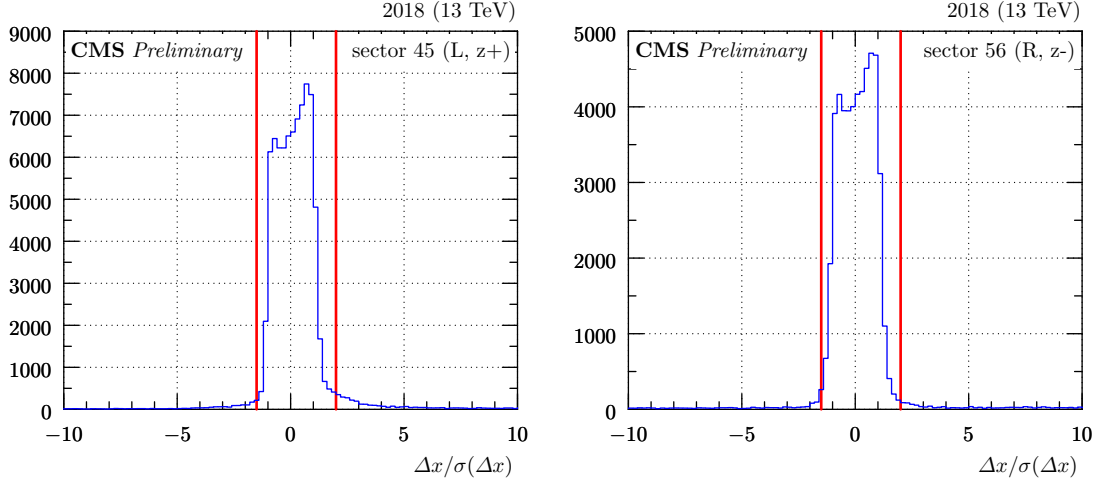
Figure 27: Association of local tracks from tracking and timing RPs (fill 7039, 2018). Δx refers to horizontal distance between the tracks from tracking and timing RPs, $\sigma(\Delta x)$ stands for the corresponding uncertainty. The vertical red lines delimit the tolerance window.
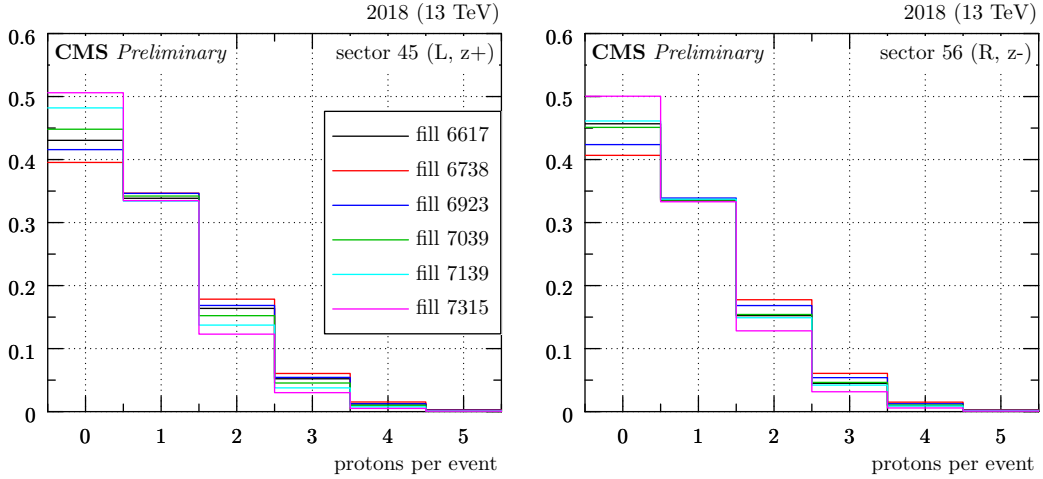

Figure 28: Multiplicity of reconstructed protons per arm and per event (2018 data). The histograms are normalised to have the integral of one. Different colours correspond to different fills as indicated in the legend. **Left**: sector 45, **right**: sector 56.

$\Delta x/\sigma(\Delta x)$ is between -1.5 and $+2.0$. This range was determined empirically to provide good efficiency and purity.

Figure 28 shows the multiplicity distributions of protons reconstructed per arm and per event. As expected, the probability decreases with increasing multiplicity. There are almost no events with five or more reconstructed protons.

Figure 29 shows the raw ξ distributions as extracted from data with no selection. Since most of the protons detected in RPs are due to pileup, the corresponding dataset has essentially no bias due to the trigger. No corrections (acceptance, efficiency, unfolding or so) have been applied to the presented distributions. The shape of the distributions is largely influenced by the acceptance, cf. red curves in Figure 32.
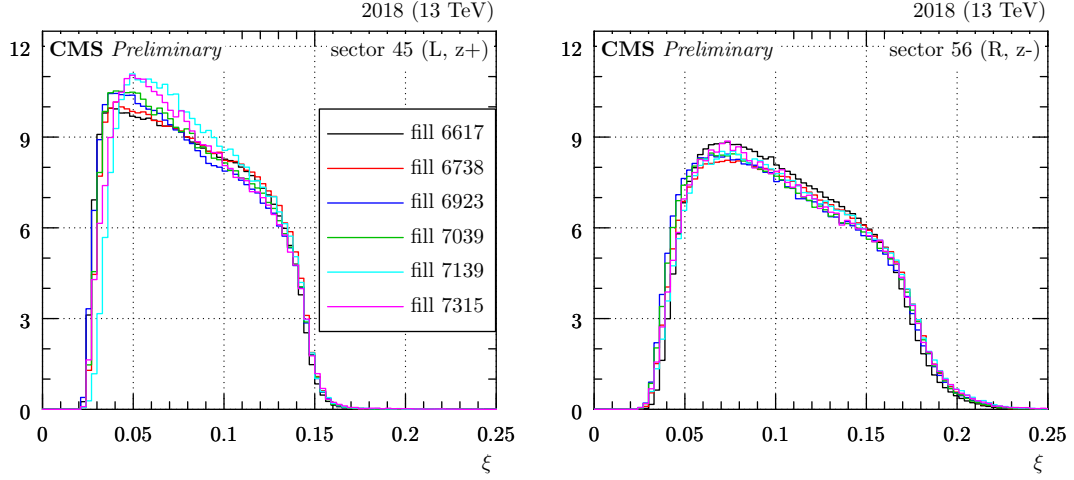
Figure 29: ξ distributions as extracted from reconstructed protons with no corrections (acceptance, efficiency, etc.), 2018 data. The histograms are normalised to have the integral of one. Different colours correspond to different fills as indicated in the legend. **Left**: sector 45, **right**: sector 56.

8 Aperture cuts

Forward protons on their way from the IP to RPs may be intercepted by various LHC aperture limitations (collimators, beam screens, etc.) which result in a detection inefficiency. These effects may be studied either by analysing the aperture constraints of all LHC elements between the IP and the RPs or empirically by searching for discontinuities in the reconstructed distributions of the proton kinematic variables. This section presents a simple study with the latter approach, performed on zero-bias data (no trigger requirement) with limited statistics.

The study is based on the distributions of the reconstructed scattering angles vs. ξ, cf. Figures 23 and 25. In both projections the data are limited in the low and high ξ region. The limitations at low ξ mostly come from the distance of the RP from the beam. This effect can be modelled by considering the distance and the shape of the sensors, as done e.g. in Section 9. The limitations at high ξ are especially sharp in the x projection, indicating that the cut arises because of horizontal constraints – a consequence of the large horizontal dispersion. The slope of the cut in the θ_x^* vs. ξ plane is given by the interplay of the horizontal dispersion and effective length optical functions at the limiting LHC element.

Figure 30 shows a typical high-ξ pattern in the θ_x^* vs. ξ distribution (qualitatively similar for all fills in Run 2), featuring a discontinuity (green markers). The discontinuity is extracted by slicing the colour-coded 2D histogram at constant θ_x^* and, for each slice, finding the ξ position of the discontinuity (each green marker corresponds to one slice). In the left plot (sector 45), the results form a two-segment line indicating possibly the presence of two relevant aperture-limiting entities. The red line represents a two-segment line fit:

$$\theta_x^* = \theta_0 + a\left(\xi - \xi_0\right), \qquad a = a_0 \text{ for } \xi < \xi_0 \text{ or } a_1 \text{ for } \xi \geq \xi_0. \tag{24}$$

In the right plot (sector 56), this simple parametrisation is compatible with the green points within the estimated uncertainty.

Figure 30 shows a significant asymmetry between sectors 45 and 56. This follows from the asymmetry of the optics: since in sector 45 the horizontal dispersion is larger, the aperture limitation is reached at smaller ξ values.
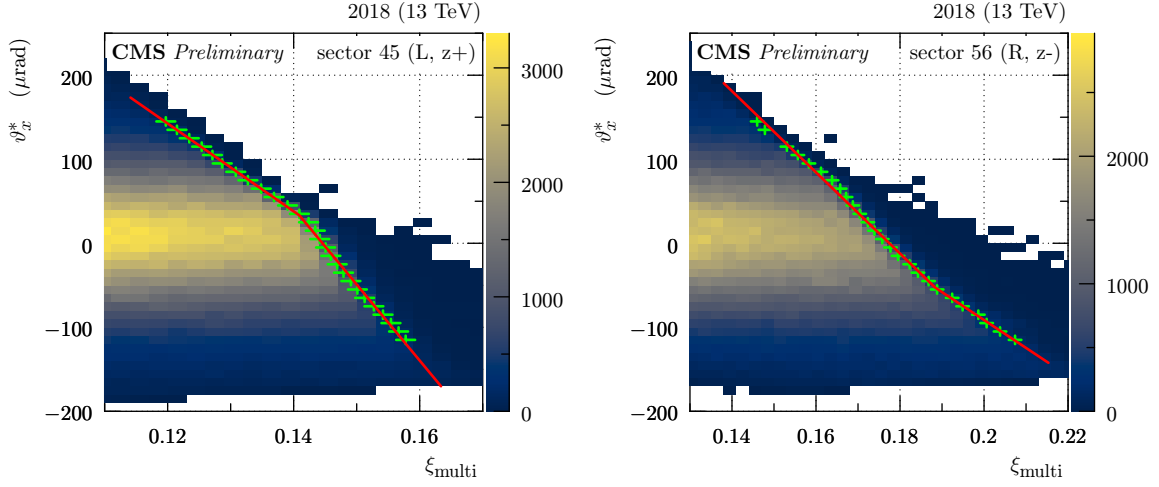
Figure 30: Distribution of θ_x^* vs. ξ reconstructed with the multi-RP method (fill 6617, 2018), zoomed at high ξ. The green markers represent the identified aperture cutoff, the red line the fit according to Eq. (24). **Left**: sector 45, **right**: sector 56.

The fit according to Eq. (24) has been performed independently on data from different fills, different crossing-angle and β^* values – in order to assess a possible dependence on these parameters. An example of such a study is shown in Figure 31. Within uncertainties, we observe almost no fill dependence (time stability) and a linear dependence on the crossing-angle (expected from the optics dependence, cf. Eq. (17)). Equivalent conclusions have been reached for other data taking periods in Run 2.

For the 2017 data, different aperture limitations have been found for the pre- and post-TS2 periods. A possible explanation is the different β^* values used for the two periods: 0.4 m and 0.3 m, respectively. On the other hand, the observed aperture difference could result from another change of the LHC configuration introduced during the technical stop. Another occasion to probe the β^* dependence of the aperture limitations is provided by the 2018 data where the β^* was changed (from 0.30 to 0.25 m) during most fills (thus less chances to introduce other changes like during a technical stop). In the 2018 data no significant difference in the apertures have been found for the two values of β^*. This can possibly be ascribed to the limited statistics used for the study or the rather modest change of β^*.

The effect of aperture limitations on PPS acceptance is illustrated in Fig. 32 for each of the years.

9 Proton simulation

This section describes a fast simulation of forward protons in PPS. On purpose, it does not simulate details (e.g. using Geant4) but focuses on higher-level observables where reproduction of features of the data is important. In particular, the simulation accounts for the following effects:

- beam smearing at the IP: vertex smearing and angular smearing (i.e. beam divergence),
- proton propagation from the IP to the centre of each RP according to the LHC optics, cf. Section 6,
- simulation of the LHC aperture limitations according to the model from Section 8,
- proton propagation between sensors in each RP: linear propagation because of the
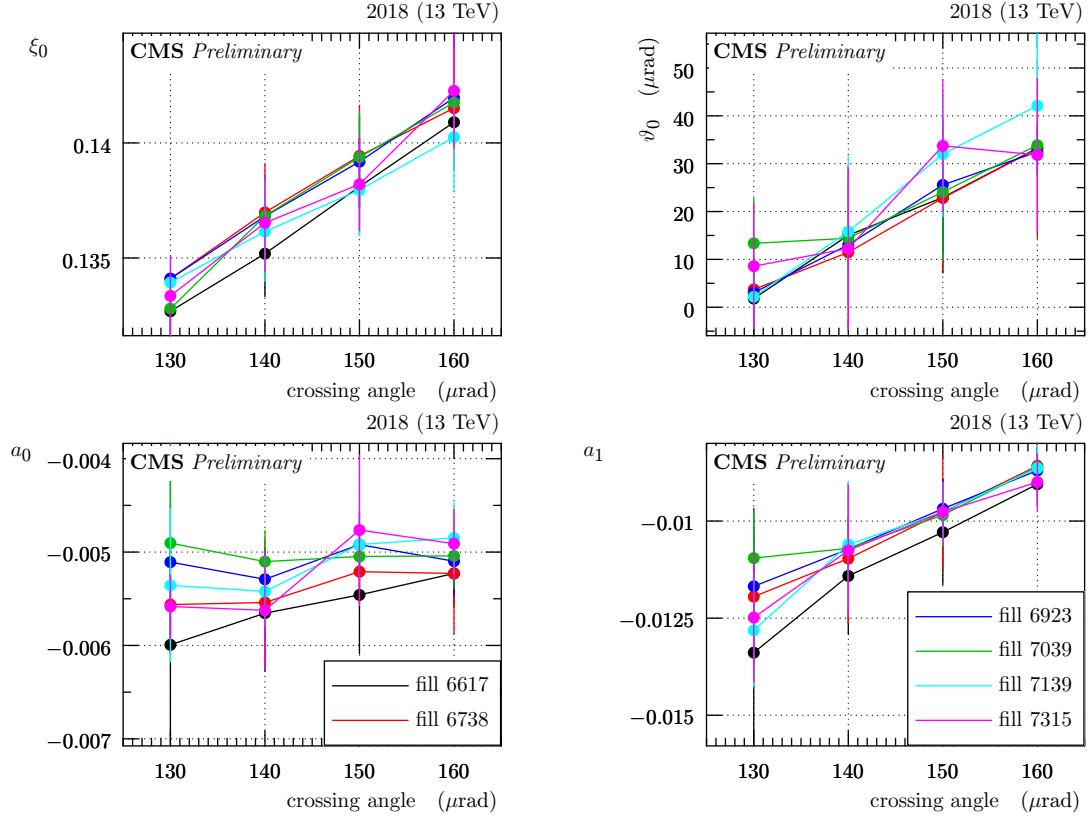
Figure 31: Summary of aperture-limitation parameters extracted from several LHC fills (different colours, 2018) and several crossing-angle values (horizontal axis), for sector 45.
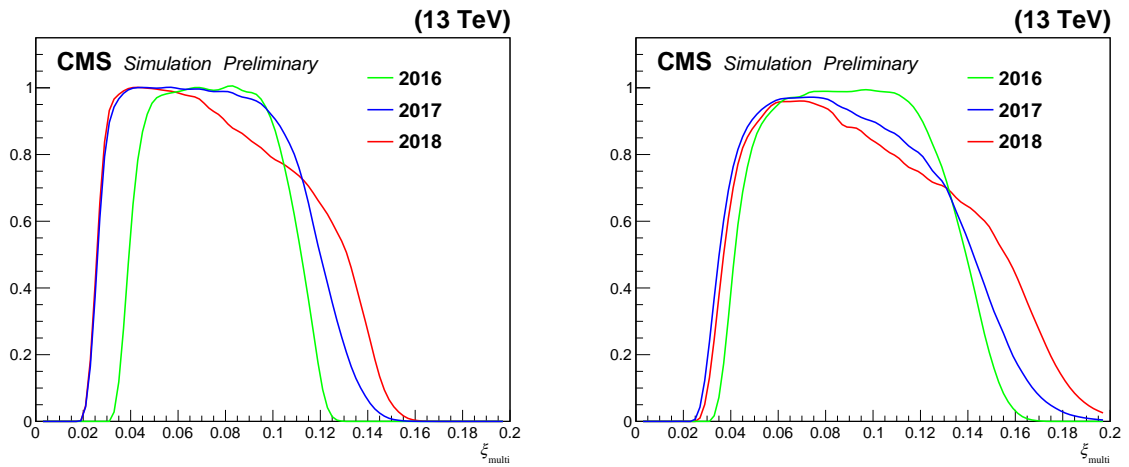

Figure 32: Fraction of reconstructed multiRP protons, as a function of ξ_{multi}, for a proton sample produced with the PPS fast simulation. Acceptance effects are taken into account.

> lack of magnetic field in the RP region,

- sensor efficiencies (optional): using efficiency maps extracted from data, cf. Section 12,

- digitisation: software hit object is created at the nearest strip/pixel – an effective pitch is used to reproduce the spatial RP resolution extracted from data,

- geometrical acceptance: check if the simulated hits are within the sensitive area of each sensor,

- for timing sensors, simulation of proton arrival time (with timing resolution extracted from data, cf. Section 13).

The hit objects created in the simulation are then processed by the standard PPS reconstruction software.

The simulation can take into account realistic distributions of parameters of importance: β^*, crossing angle, optics, RP positions, apertures, resolution and efficiencies. The values of crossing angle and β^* are randomly sampled from the 2D histograms extracted from the data, cf. Figure 2. Varying RP positions reflect the movements performed during the LHC operation: e.g. vertical RP movements in the technical stops of 2018 to distribute the radiation damage. For consistency between simulation and data, the simulation conditions are randomly switched with the frequency extracted from data (following integrated luminosities).

The simulation can be used with whatever source of simulated forward protons. By default, the simulation uses a particle gun which generates random protons with a uniform ξ distribution and Gaussian θ_x^* and θ_y^* distributions with zero mean and RMS of $60\,\mu$rad. These settings simulate minimum bias protons.

The beam divergence, σ_{bd}, used in the simulation has been extracted from data with three complementary methods. First, the beam divergence can be estimated from the beam emittance, ϵ, measured by the LHC: $\sigma_{\mathrm{bd}} = \sqrt{\epsilon/\beta^*}$. The second estimate is obtained from the beam-spot size, σ_{bs} measured by the CMS central detector: $\sigma_{\mathrm{bd}} = \sigma_{\mathrm{bs}}\sqrt{2}/\beta^*$. The factor of $\sqrt{2}$ stems from converting the beam-spot size (product of two beams) to the single-beam width, cf. Eq. (10). The third method is the most direct, but can only be applied to data from the special "alignment" fills where a sample of elastically scattered protons can be selected. In the final state of elastic scattering there are two protons, ideally with exactly opposite directions. As the direction fluctuations are predominantly caused by the divergence, the size of the latter is determined from the RMS of scattering angle differences between the two elastic protons. All the methods agree on a beam divergence of about $30\,\mu$rad.

Multiple validations have been performed to check whether the simulation reproduces observations; an example is shown in Figure 33. In the left plot, the simulation describes well the cutoff at low x (due to the sensor edge) and the smooth cutoff at large x (due to the LHC aperture limitations). In the right plot, the simulation describes well the cutoff at large y (due to the sensor edge).

An example of timing simulation is shown in Figure 34. Here, a realistic timing resolution is used for the reconstructed protons (vertical axis), but perfect vertex z (horizontal) reconstruction is assumed.
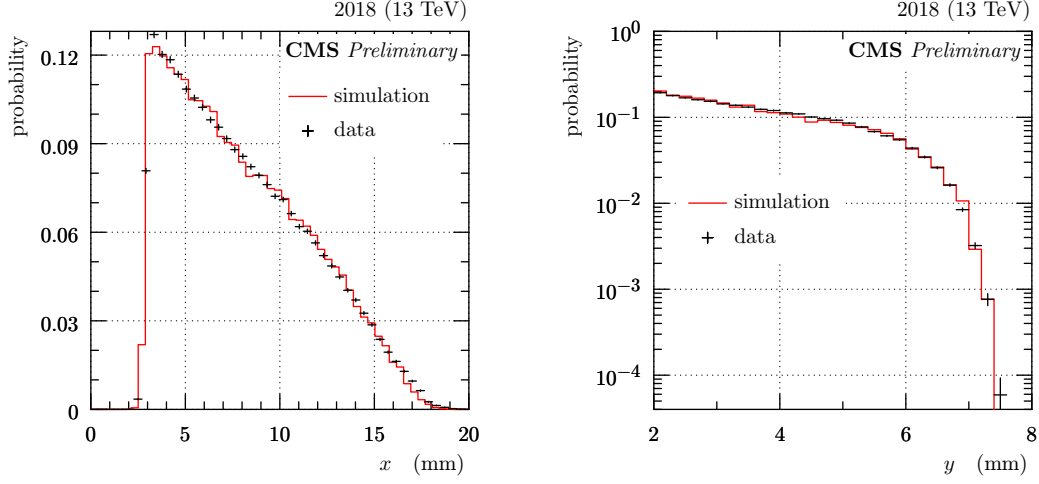
Figure 33: Comparison of hit distributions from simulation (red) and LHC data (fill 6738, no explicit event/track selection, black), for 2018 pre-TS1 configuration and the near RP in sector 56. **Left**: distribution of horizontal track positions, **right**: distribution of vertical track positions (y range limited to the area around the upper sensor edge).
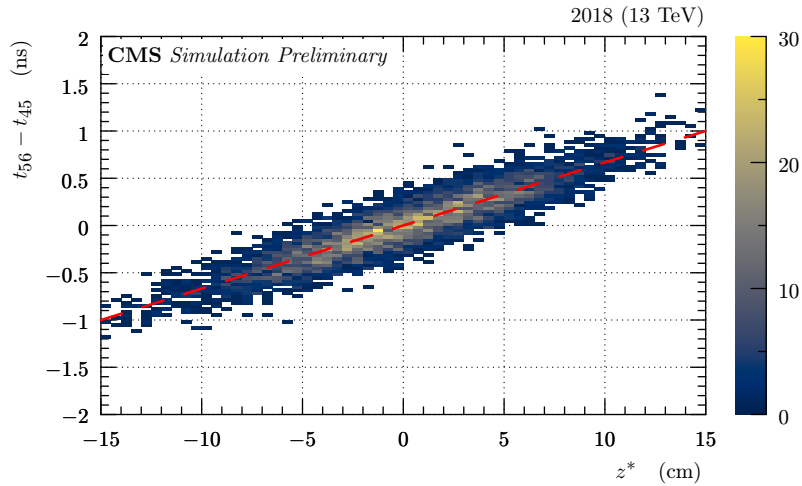

Figure 34: Simulated correlation between vertex position along the beam, z^*, and the proton timing difference observed in LHC sectors 56 and 45 (2018 pre-TS1 configuration). Reconstruction resolution of z^* is not included in this plot. The red dashed line indicates the ideal correlation.

10 Uncertainties

Since the simulation described in Section 9 reproduces well the data (see e.g. Figure 33), it can be used to benchmark the performance of the proton reconstruction presented in Section 7. The performance will be characterised in terms of the three quantities below.

- "**Bias**" = mean of reconstruction - truth. This may occur e.g. due to effects neglected by the reconstruction formula; a notable example is the single-RP reconstruction of ξ, Eq. (22), which is unable to correct for the effect of the horizontal scattering angle θ_x^*. The "bias" may be non-zero even with a perfect knowledge of the conditions (alignment, optics, etc.).

- "**Resolution**" = RMS of reconstruction - truth. This may occur due to random event-to-event fluctuations, e.g. from finite sensor resolution or non-perfect separation of kinematics variables in the reconstruction. A notable example of the latter can again be the single-RP reconstruction of ξ: since this reconstruction is biased by a term proportional to θ_x^*, the event-to-event fluctuations in the scattering angle effectively lead to a degraded ξ resolution. The "resolution" may be non-zero even with a perfect knowledge of the conditions.

- "**Systematics**" = effect of biased conditions. The "systematics" may be non-zero even if "bias" and/or "resolution" vanish.

The considered sources of conditions bias include:

- alignment: following the uncertainties from Table 3, perturbations of the horizontal and vertical alignment have been studied separately. Furthermore, symmetric (same sign in near and far RP) and anti-symmetric (opposite sign in the two RPs) shifts have been considered.

- optics: uncertainties of the horizontal effective length, L_x, (cf. Figure 18, left), its derivative dL_x/ds (cf. Figure 18, right) and the horizontal dispersion giving the function x_d (cf. Table 5).

The results presented here were obtained with the fast simulation described in Section 9 and its default settings which reproduce well the zero-bias data, in particular with the θ_x^* distribution given by a convolution of two Gaussians, one representing the physics scattering (with an RMS of 60 μrad) and one representing the beam divergence (with an RMS of 30 μrad).

The MC-based results from the fast simulation are compared to semi-analytic calculations. These provide a validation (good agreement is found) and a detailed insight in the mechanisms producing certain trends in results, as discussed later.

Below, we show results for the period 2018 pre-TS1 and for the detector arm in sector 56. These can be considered as typical since the results for other periods and the other arm are qualitatively similar. We systematically show separately the results for single- and multi-RP reconstruction as rather different characteristics are expected. For brevity we focus on the results of ξ reconstruction. Some results for the reconstructed four-momentum transfer squared, t, are shown at the end of this section.

Figure 35 gives an example of resolution studies. For single-RP reconstruction (left plot), the resolution is dominated by the neglected angular term ($L_x(\xi)\,\theta_x^*$) in the proton propagation. The RMS grows with ξ because the horizontal effective length, $L_x(\xi)$, grows (in absolute value) with ξ (cf. Figure 15). At very high ξ, the width of the θ_x^* distribution within detector acceptance is reduced by the LHC collimators (cf. Section 8). Therefore fluctuations in reconstruction
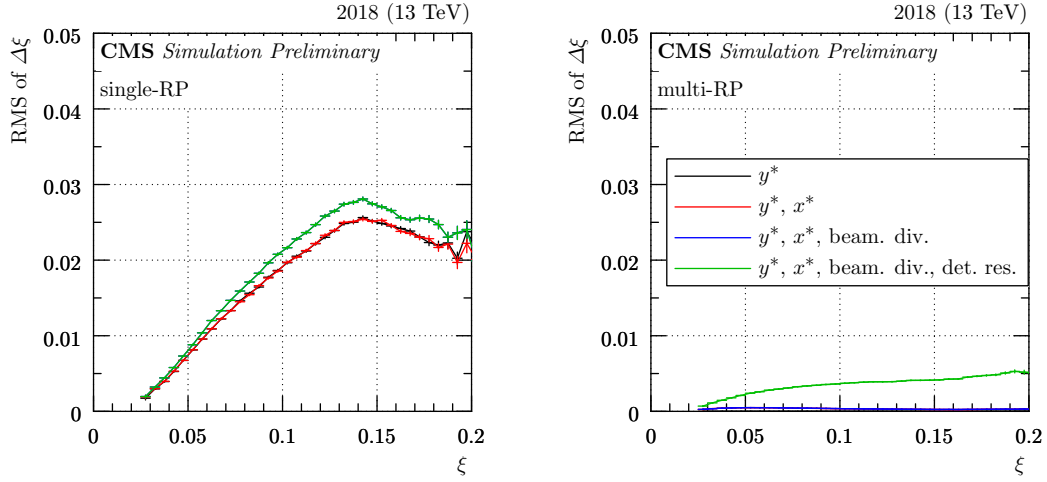
Figure 35: Example of resolution studies for ξ (2018 pre-TS1, sector 56). On the vertical axes, $\Delta\xi$ refers to the difference between the reconstructed and simulated ξ. On the horizontal axes, ξ denotes the simulated value. The different colours refer to different smearing effects considered. Black: only vertical vertex smearing, red: in addition also horizontal vertex smearing, blue: in addition also beam divergence, green (the most complete scenario): in addition also detector spatial resolution. Note that some curves are superimposed. **Left**: single-RP, **right:** multi-RP reconstruction.

are reduced, which however leads to a bias (quantified in Figure 36). For the multi-RP reconstruction (right plot), the only sizeable contribution to the resolution comes from the detector spatial resolution. This explicitly justifies the statement that neglecting the horizontal vertex, x^*, in the reconstruction makes a negligible effect, cf. Section 7.

Figure 36 shows an illustration of the bias studies. The single-RP reconstruction (left plot) is significantly biased close to the acceptance edges (very low and very high ξ). At these edges the accepted θ_x^* range becomes strongly asymmetric and since the θ_x^* term is neglected in single-RP reconstruction, the bias appears. The bias is negligible for multi-RP reconstruction (right plot).

Figure 37 shows an example of the biased-conditions studies. The individual curves show the systematic error in the reconstruction of ξ caused by various conditions biases at $1\,\sigma$ level (cf. the list above). For both single-RP (left plot) and multi-RP (right plot), the leading contribution (magenta) stems from the uncertainty of the horizontal dispersion. The change of behaviour at large ξ is due to the LHC aperture limitations which modify/restrict the distribution of protons within the RP acceptance. The single-RP reconstruction (left plot) has very low sensitivity to certain scenarios, e.g. the blue and cyan one. The multi-RP reconstruction (right plot) is more sensitive to systematic errors, especially at very high ξ.

Since the contributions shown in Figure 37 are statistically independent, they can be combined in quadrature to obtain the total uncertainty, as shown in Figure 38. Up to $\xi \approx 0.15$, the uncertainties of the single-RP (red) and the multi-RP (blue) reconstruction are very similar.

A summary of all the studies presented in this section is provided in Figure 39. The comparison of the single-RP (left plot) to the multi-RP reconstruction (right plot) shows that the former has significantly larger bias, significantly worse resolution and almost comparable systematics – being better only in the high-ξ region. This plot justifies the general preference for the multi-RP reconstruction.

Besides ξ, PPS can also estimate the four-momentum transfer squared, t, of protons reaching
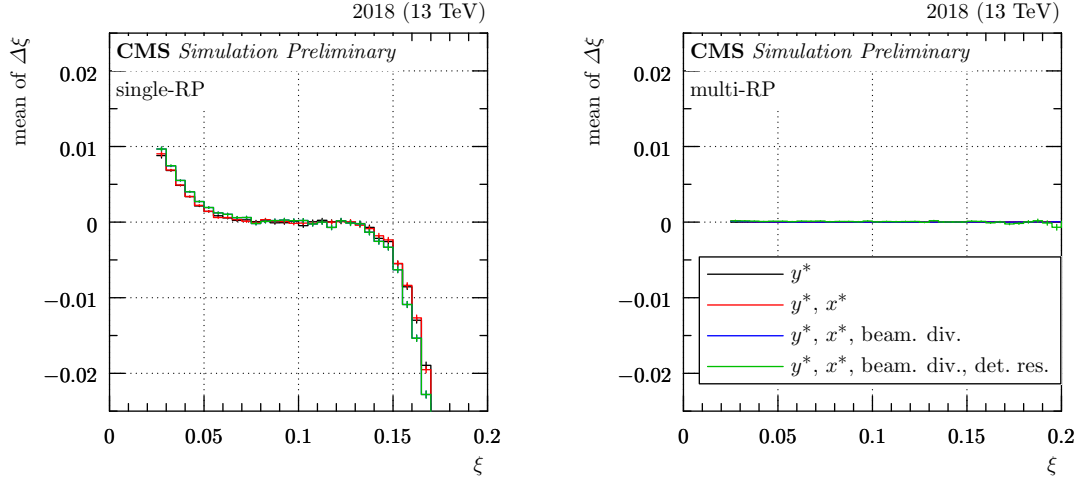
Figure 36: Example of bias studies for ξ (2018 pre-TS1, sector 56). The different colours refer to different smearing effects considered (see caption of Figure 35). **Left**: single-RP, **right:** multi-RP reconstruction.
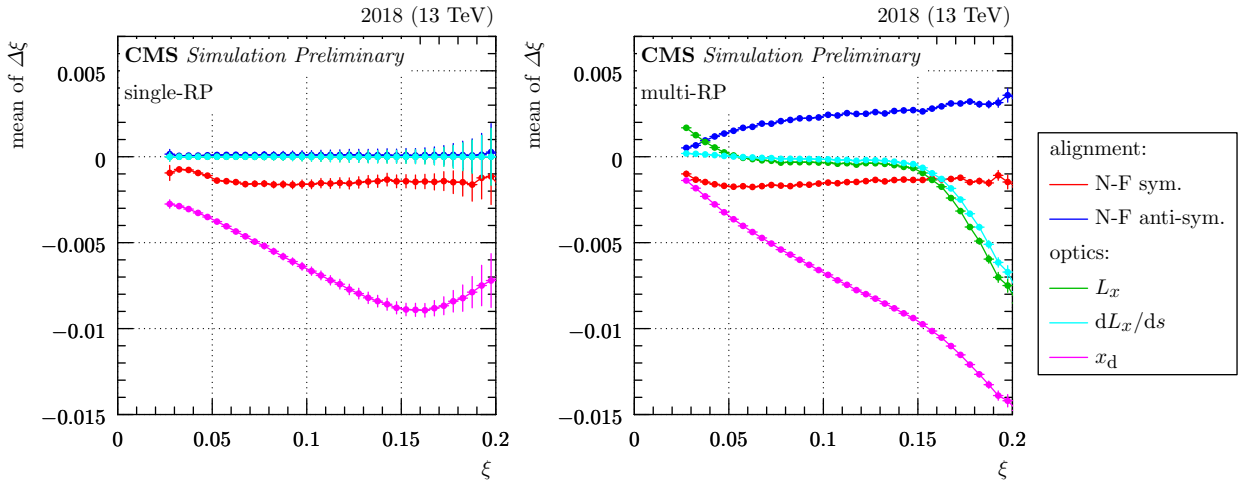

Figure 37: Example of systematic studies for ξ (2018 pre-TS1, sector 56). Each curve corresponds to a perturbation at $1\,\sigma$ level. The red and blue curves represent alignment perturbations: in the former both the near and far RP are shifted in the same direction, in the latter opposite directions are considered. The remaining scenarios cover perturbations of the optical functions. **Left**: single-RP, **right:** multi-RP reconstruction.
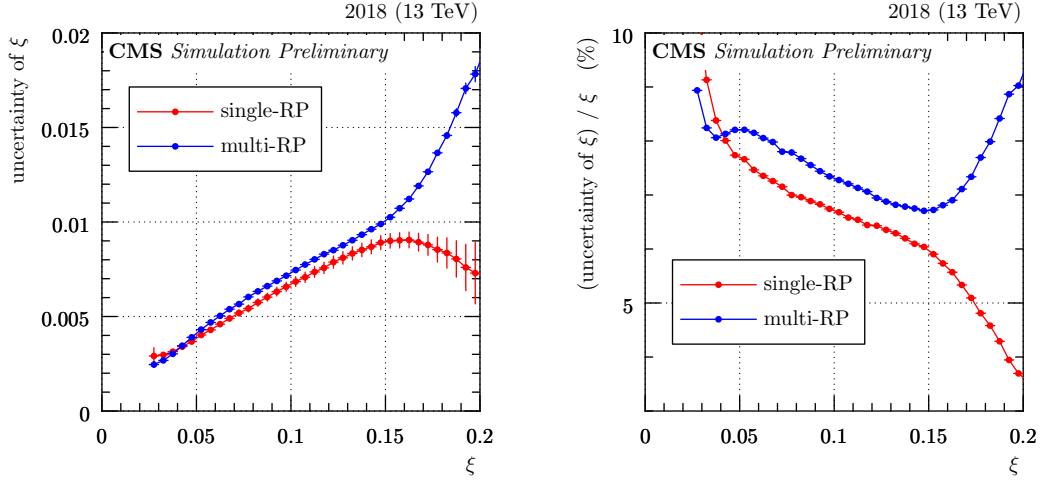
Figure 38: Example of combined systematic uncertainties of proton ξ (2018 pre-TS1, sector 56). The results for the single-RP and multi-RP reconstructions are shown in red and blue, respectively. **Left**: absolute, **right:** relative uncertainty.

Figure 39: Comparison of bias, resolution and systematics characteristics (2018 pre-TS1, sector 56). For the bias and resolution curves, all considered smearing effects are included. The systematics curves represent the combination of all contributions.

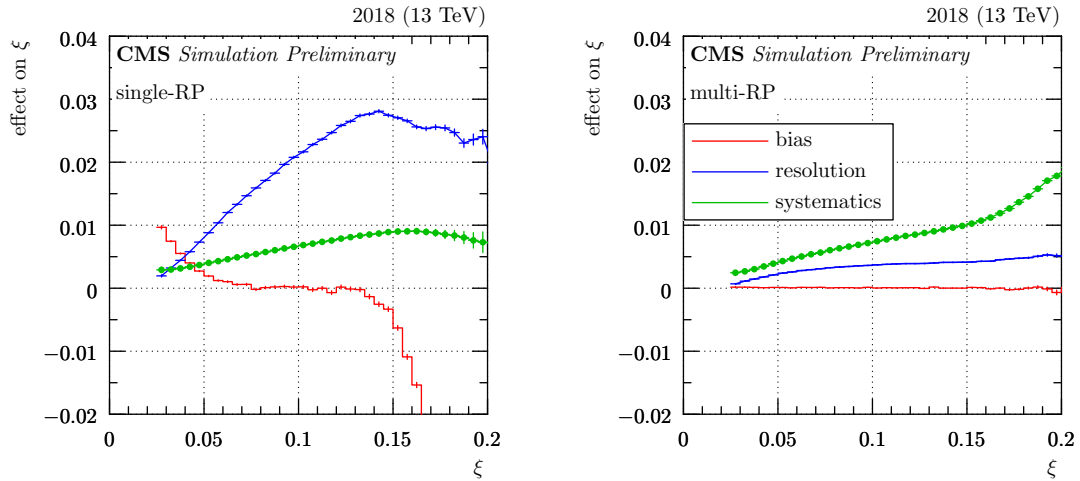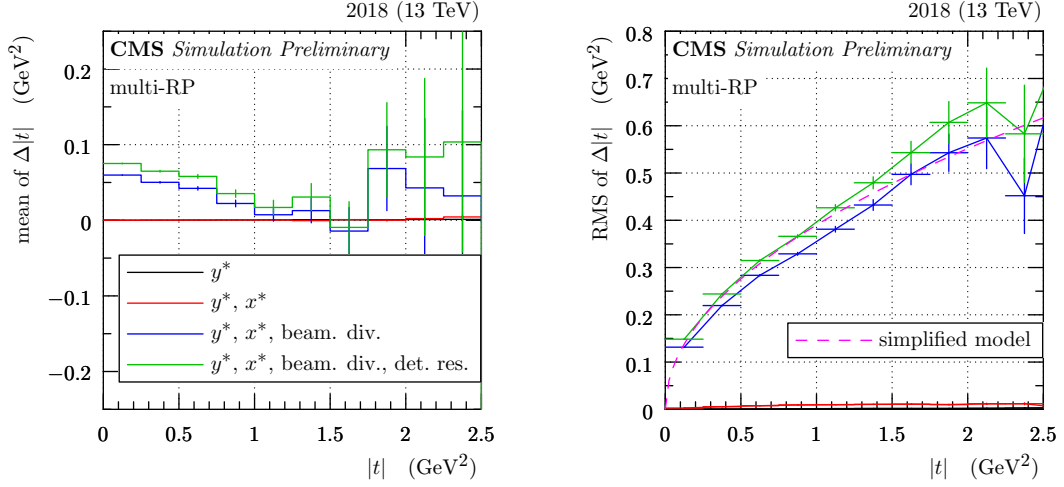Figure 40: Example of resolution bias (left) and resolution (right) studies for four-momentum transfer squared, t, with multi-RP reconstruction (2018 pre-TS1, sector 56). On the vertical axes, $\Delta|t|$ refers to the difference between the reconstructed and simulated value of $|t|$. On the horizontal axes, $|t|$ denotes the simulated value. The different colours refer to different smearing effects considered. Black: only vertical vertex smearing, red: in addition also horizontal vertex smearing, blue: in addition also beam divergence, green (the most complete scenario): in addition also detector spatial resolution. In the right plot, the dashed magenta curve represents the simplified analytic model from Eq. (27).

the RP detectors. Formally, this quantity is defined as $(P' - P)^2$, where the four momenta P and P' are those before and after the collision, respectively. It can be related to other kinematic variables:

$$t = t_0(\xi) - 4p_{\text{nom}}^2(1 - \xi)\sin^2\left(\frac{\sqrt{\theta_x^{*2} + \theta_y^{*2}}}{2}\right) ,$$

$$t_0(\xi) = 2\left(m^2 + p_{\text{nom}}^2(1 - \xi) - \sqrt{(m^2 + p_{\text{nom}}^2)(m^2 + p_{\text{nom}}^2(1 - \xi)^2)}\right) . \tag{25}$$

Since t depends strongly on the scattering angles, it only makes sense to estimate it with the multi-RP reconstruction (with the single-RP approach θ_x^* is not available at all and for θ_y^* only a crude estimate is made). Typical examples of t reconstruction bias and resolution are shown in Figure 40. The smearing effect with the largest impact is the beam divergence (cf. the difference between the red and blue curves), followed by the spatial resolution of the sensors (cf. the difference between the blue and green curves).

As shown in Figure 40, left, there is a non-zero bias in t reconstruction, mostly due to the beam divergence. Formally, the beam divergence causes a smearing in scattering angles: $\theta_{x,y}^* \rightarrow \theta_{x,y}^* + \Delta\theta_{x,y}^*$, where the standard deviation of $\Delta\theta_{x,y}^*$ is given by the beam divergence, σ_{bd}. Inserting this into Eq. (25) one can obtain the beam-divergence effect on $|t|$ – the difference in $|t|$ with and without beam divergence in the approximation of small scattering angles:

$$\Delta|t| \approx p_{\text{nom}}^2(1 - \xi)\left[2\theta_x^*\Delta\theta_x^* + 2\theta_y^*\Delta\theta_y^* + \Delta\theta_x^{*2} + \Delta\theta_y^{*2}\right] . \tag{26}$$

Since $\Delta\theta_{x,y}^*$ are expected to fluctuate symmetrically about zero, the first two terms in the square brackets yield a strongly suppressed contribution to the mean value of $\Delta|t|$. Conversely, the last two terms are always non-negative and therefore give rise to the reconstruction bias: $\Delta|t| \approx$

$2p_{\text{nom}}^2(1-\xi)\sigma_{\text{bd}}^2$. For $\xi = 0$, this simple model gives mean $\Delta|t| \approx 0.08\,\text{GeV}^2$, thus well comparable with results in the figure. The non-flat shape reported in the figure is due to the limited acceptance of the RP detectors and the near-far association cuts (cf. Section 7) applied in the proton reconstruction.

Figure 40, right, shows the $|t|$ resolution which deteriorates with increasing $|t|$. This can be expected from Eq. (26), particularly from the first two terms in the square brackets where the beam divergence fluctuations are scaled with the scattering angles. Neglecting the other terms in the square brackets, one can derive the functional dependence of the $|t|$ resolution

$$\text{RMS of } \Delta|t| \approx 2p_{\text{nom}}\sqrt{1-\xi}\,\sqrt{|t|}\,\sigma_{\text{bd}}\,, \tag{27}$$

which is well compatible with the plot.

11 Validation with dimuon sample

As a final check of the proton reconstruction, the calibrations and reconstruction algorithms described in the previous sections are applied to a control sample of $\gamma\gamma \rightarrow \mu^+\mu^-$ events with at least one intact proton (Fig. 41), using the 2017 and 2018 data.
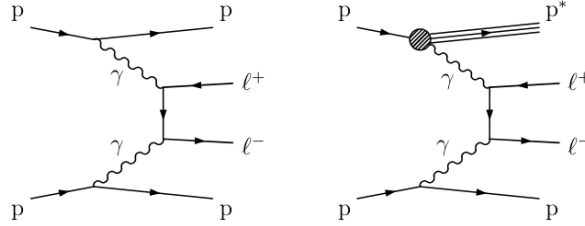

Figure 41: Diagrams for $\gamma\gamma \rightarrow \mu^+\mu^-$ production with intact protons. Left: fully exclusive production, with both protons remaining intact. Right: Single proton dissociation, with one of the two protons remaining intact.

As described in Refs. [34, 38], the value of ξ in signal events can be inferred from the muon pair via the expression:

$$\xi(\mu^+\mu^-) = \frac{1}{\sqrt{s}}\left[p_T(\mu^+)e^{\pm\eta(\mu^+)} + p_T(\mu^-)e^{\pm\eta(\mu^-)}\right], \tag{28}$$

with the $\pm\eta$ solutions corresponding to the case where the protons are moving in the $\pm z$ direction, respectively.

The offline event selection in the central detectors is identical to that of Ref [34]. Two oppositely charged muons are required, passing standard tight identification criteria, and with $p_T > 50$ GeV. In order to exclude the region dominated by resonant $Z \rightarrow \mu^+\mu^-$ production, an invariant mass requirement of $m(\mu^+\mu^-) > 110$ GeV is also imposed. Finally, in order to enhance the (semi-) exclusive production processes, selections are applied to the track multiplicity at the dimuon vertex, and to the acoplanarity ($a = 1 - |\Delta\phi(\mu^+\mu^-)|/\pi$) of the muons. The track multiplicity selection is applied by fitting the two muons to a common vertex, and requiring that no additional charged tracks are present within 0.5 mm of the vertex position. Back-to-back muons, characteristic of the signal process, are selected by requiring $a < 0.009$.

The protons reconstructed with the single-RP and multi-RP algorithms in these events are then examined, to look for correlations with the muons. In each event, the two solutions, corresponding to the two arms of the spectrometer, are considered separately. In the 2018 data it is

possible to reconstruct more than one proton per arm; for this study, in order to limit the combinatorial backgrounds, we require no more than one proton to be reconstructed in the arm of interest. Backgrounds are expected to arise from real dimuon production (from Drell-Yan or $\gamma\gamma \to \mu^+\mu^-$ events with double proton dissociation), in combination with unrelated protons from other collisions in the same bunch crossing ("pileup").

In Ref [34], this procedure was applied to the 2016 data, in both the $\mu^+\mu^-$ and e^+e^- final states. While the smaller integrated luminosity did not allow detailed studies, a combined $> 5\sigma$ excess of correlated events was observed using the single-RP algorithm, compatible with the predicted signal. With the 2017 and 2018 data, approximately 10 times more single-RP $\mu^+\mu^-$ events are available, permitting more refined studies with this sample.

Figure 42 shows the resulting two-dimensional scatter plots from the 2017 and 2018 data, separately for the two arms and the two years. The shaded bands indicate the approximate region that is kinematically inaccessible for signal events, as the protons would be outside the acceptance. These regions can be populated by background events where a dimuon event is combined with an unrelated proton from a pileup interaction. In the remaining area of the plots, a clear clustering of events around the diagonal, where a fully correlated signal would be expected, is visible for both arms and years. The samples extend to $\xi \sim 0.12$; no significant deviation from the diagonal is observed in this region. The difference between the two proton reconstruction algorithms can be seen from the plots. The multi-RP algorithm gives a narrower distribution around the diagonal and fewer off-diagonal background events, while the single-RP algorithm extends the coverage to lower ξ values.

In order to compare more quantitatively the data with simulation, a one-dimensional projection in the variable $1 - \xi(p)/\xi(\mu^+\mu^-)$ is performed, combining both arms and years, for events with $\xi(\mu^+\mu^-) > 0.04$. The expected shape of the residual background is obtained from a sideband region in the acoplanarity ($0.009 < a < 0.1$) and extra tracks multiplicity ($5 < N < 10$). The expected signal shape is obtained from a simulated sample of $\gamma\gamma \to \mu^+\mu^-$ events with both protons intact. A full simulation of the central CMS detectors is performed, while the direct simulation described earlier is used for the protons. For the simulation, a mixture of LHC crossing angles and PPS configurations proportional to the integrated luminosity of each data-taking condition is used. The background shape is normalised to the data in the range $|1 - \xi(p)/\xi(\mu^+\mu^-)| > 0.5$. The signal simulation is then normalised to the difference between the data and the background in the range $|1 - \xi(p)/\xi(\mu^+\mu^-)| < 0.5$.

The resulting projections are shown in Fig. 43, with the data first compared to the sum of the signal and background components, and then to the signal shape after subtracting the background, in a narrower range. In the background-subtracted plot, the systematic uncertainties on ξ are indicated by light shaded bands on the simulation, corresponding to the cases where the reconstructed ξ is shifted up or down by the systematic uncertainty. The width of the signal peak in the data is well reproduced by the simulation ($\sim 4.8\%$, including a sub-leading contribution of $\sim 1.8\%$ from the muon resolution, estimated from simulation), indicating that the ξ resolution is well described. The peak position is slightly shifted (by $\sim 4\%$), but well within the error bands, indicating any residual effect is compatible with the known systematics.

In summary, the PPS multi-RP reconstruction has been used to study $\gamma\gamma \to \mu^+\mu^-$ events with at least one final-state proton, in the kinematic range $m(\mu^+\mu^-) > 110$ GeV and $\xi > 0.04$. A good correlation between $\xi(\mu^+\mu^-)$ and the ξ of the protons is observed in the data up to $\xi \sim 0.12$; the mean and width of the signal distribution are reproduced by the simulation, within the known systematic uncertainties. This indicates that the optics, alignment, and related systematics of the proton ξ reconstruction are well understood for the data collected dur-
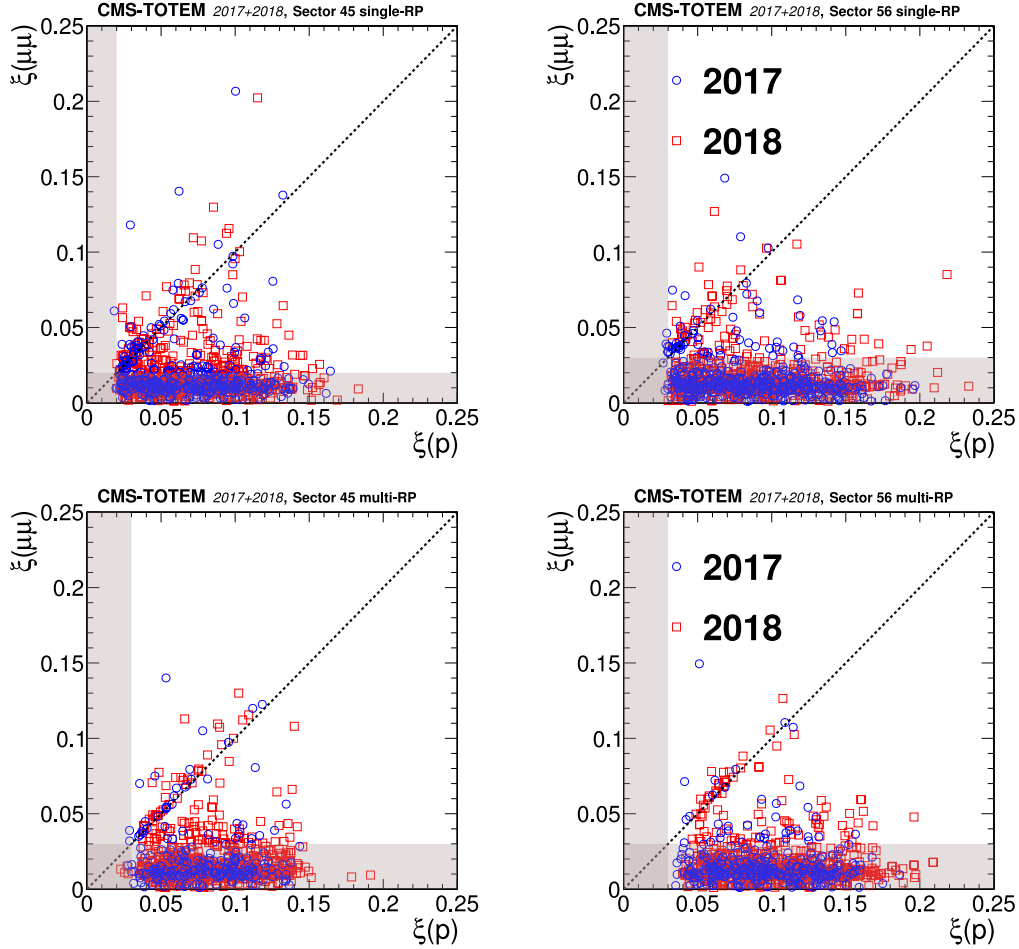
Figure 42: Distribution of $\xi(p)$ vs. $\xi(\mu^+\mu^-)$ for the $z > 0$ (LHC sector 45) and $z < 0$ (LHC sector 56) directions in the CMS coordinate system. The two styles of points represent the data collected during 2017 and 2018. The shaded bands represent the region incompatible with the PPS acceptance for signal events; events in this region are expected to arise from random combinations of muon pairs with protons from pileup interactions. The upper plots show the results of the single-RP reconstruction algorithm, while the lower plots show the multi-RP results. The dotted line illustrates the case of a perfect correlation, where signal events are expected.

ing 2017 and 2018, in addition to the previously studied 2016 data [34].

12 PPS tracking efficiency

The efficiency of the PPS tracking detector needs to be closely monitored, as radiation-induced effects can degrade the performance along the operation.

Multiple factors need to be taken into account: the efficiency of the detectors, the reconstruction algorithm efficiency, and the probability that the proton interacts with the material between the two tracking stations, and cannot be measured.

PPS used multiple detector technologies during the data-taking, and the definition of the efficiency changes accordingly.
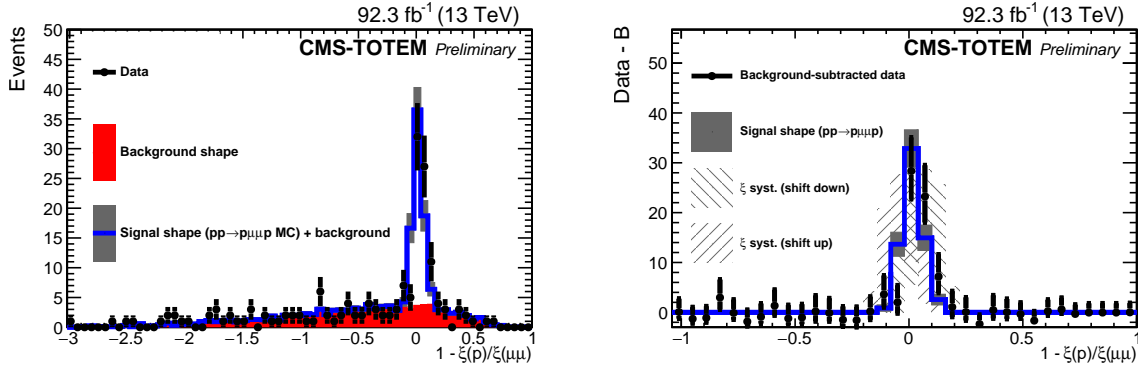
Figure 43: One-dimensional projections of the correlation between $\xi(p)$ and $\xi(\mu^+\mu^-)$, for the full 2017+2018 data sample and both arms combined, using the multi-RP algorithm. A minimum requirement of $\xi(\mu^+\mu^-) > 0.04$ is applied. The left plot shows the data compared to the background shape (solid histogram) estimated from sideband regions, and the signal shape obtained from simulation (open histogram). The right plot shows the data and signal shape in a narrower region, after subtracting the background component from the data. In the right plot the dark bands represent the uncertainty due to simulation statistics, while the two light shaded bands represent the effect of shifting the distribution up or down by the systematic uncertainty of the proton ξ reconstruction.

In 2016, with only strip detectors used, allowing only one proton track to be reconstructed in each station, the reconstruction algorithm efficiency is close to 100%, as loose association cuts can be used (cf. Section 7). The dominant role is played by detector effects, such as radiation damage and multi-tracking inefficiency. A more detailed description is given in Section 12.1.

In 2017 and 2018, pixel detectors could resolve multiple tracks in the same station, and a different approach for the efficiency estimation is used. The reconstruction efficiency for multiRP protons was split into two independent multiplicative factors: the efficiency of the "near" detector and the so-called multiRP efficiency. The former takes into account only the detector-related effects for the near RP, while the latter accounts for detector-related efficiency in the far RP, the reconstruction algorithm efficiency, and the proton propagation. The first factor is derived as described in Sections 12.1 and 12.2, while the second is discussed in Section 12.3.

Efficiency corrections are computed for each RP and data-taking period separately.

12.1 Silicon strip detector efficiency

Two main sources of inefficiency affect the PPS strip detectors: radiation damage and the presence of multiple tracks in the same event. These effects have been studied separately and are described with two efficiency factors.

If more than one particle produces signal in the strip detectors, track candidates that do not correspond to a real particle, the so-called ghost tracks, will be found. Because of this, strip detectors can only be used in events where one track is present [39].

In minimum-bias samples, events with one or more protons in the strip detectors are selected. This is done by requiring either at least one track pattern in both strip orientations, or a number of detector hits greater than the maximum allowed by the pattern-recognition algorithm, which is tuned to accept a single proton track with some tolerance for detector noise. The selected events are used to compute the efficiency factor, which is the ratio between the number of reconstructed tracks and the number of selected events. This efficiency factor is inversely
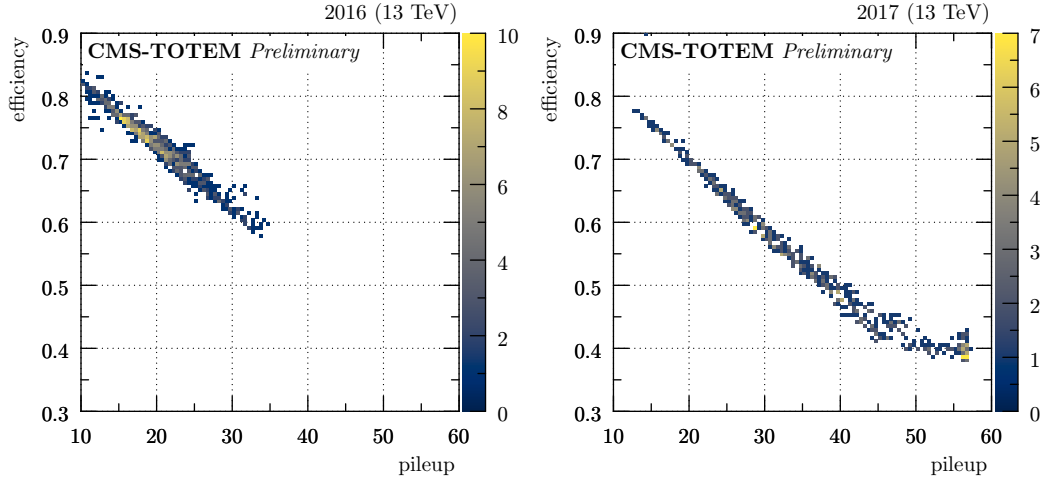
Figure 44: Strip multiple track efficiency component versus pileup in the sector 45 near RP. **Left:** data-taking period between the first and the second 2016 Technical Stops. **Right:** data-taking period between the second and the third 2017 Technical Stops.

related to the pileup, and ranges between 40% and 80%. Consistent results are observed in both 2016 and 2017, and across different sectors, and illustrated in Figure 44.

The second factor takes into account time-dependent effects produced by radiation, and it has been studied with a tag-and-probe method [40]. In order to probe the efficiency of the strip detectors in one station, minimum-bias events with one reconstructed track in the other RP (tag) of the same arm, passing loose quality criteria, are selected. Events with more than one recognized track pattern in the strip detector being probed are excluded, together with events with multiple tracks in the tag RP, in case of pixel detectors. A matching window of $|\Delta\xi| < 0.01$ is defined, where $\Delta\xi$ represents the difference between the single-RP ξ measurement associated with the track in the tag RP, and the measurement in the RP being probed, if a track is detected.

The efficiency correction factor is defined as the ratio between the number of events in which a strips track satisfies this matching criterion, and the total number of events selected. Statistical uncertainties have been found negligible, and two sources of systematic uncertainty have been evaluated. A 1% uncertainty is associated to the choice of the minimum-bias sample used for the estimation; an uncertainty of the same size is associated to the variation of the quality criteria applied to the tagging track. A larger (10%) conservative systematic uncertainty is applied to 2016 efficiency factors because a different method is used. Efficiencies are derived by comparing ξ distributions in data with respect to the ones observed in the alignment fill, when the detectors had not suffered any radiation damage yet. The uncertainty is estimated by comparing with results obtained with the tag-and-probe method.

Figure 45 shows the results as a function of the x-y global coordinates of the track measured in the tagging RP, for the region covered by the detector acceptance and below the collimator aperture limits. The area damaged by radiation is clearly visible and its size and inefficiency grows with the integrated luminosity. However, efficiency measurements show average values higher than 95% in the rest of the detector area. Similar results are observed in the 2016 data, although the lower collected integrated luminosity reduced radiation effects. Data-taking periods in which strips detectors were not inserted or operational are excluded from the presented results. They mainly affect the last period of 2017 (bottom-right plot of Fig. 45), where they account for ≈ 10 % efficiency loss.
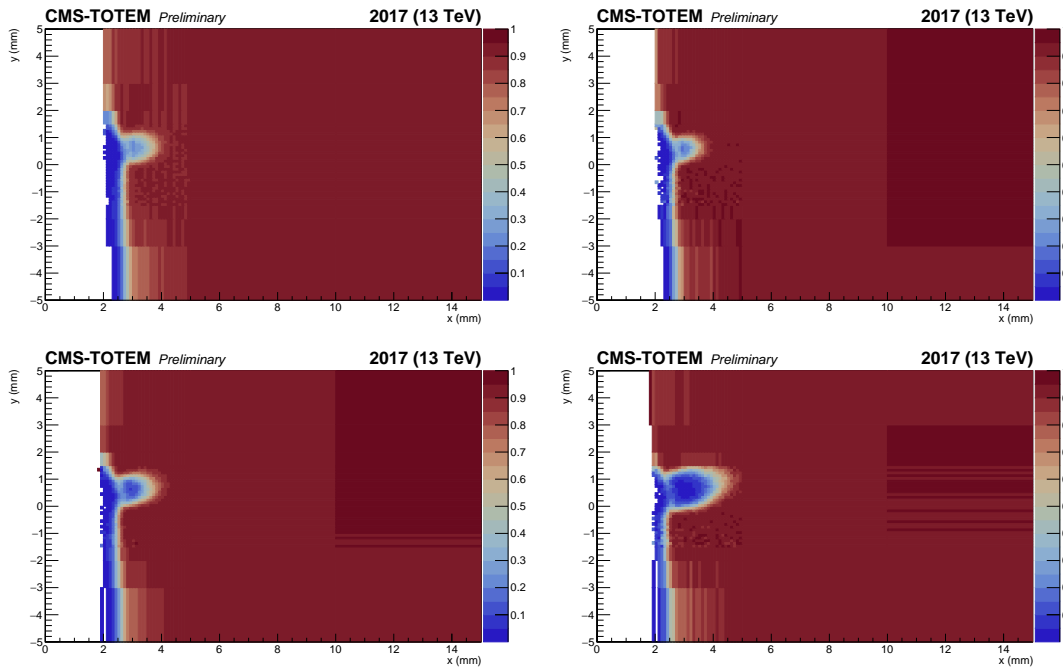
Figure 45: Strip detector tracking efficiency component related to radiation effects, computed with data collected in 2017, over different consecutive data-taking periods. The figure shows the results for the 2017 sector 56 near station, as a function of the *x-y* global coordinates of the track measured in the tagging far station, for different periods. Each period is defined as an interval in integrated luminosity computed since the detector installation.
Top left: $L_{INT} = 0$–9 fb^{-1}. Top right: $L_{INT} = 9$–10.7 fb^{-1}. Bottom left: $L_{INT} = 10.7$–18.5 fb^{-1}. Bottom right: $L_{INT} = 18.5$–22.2 fb^{-1}.
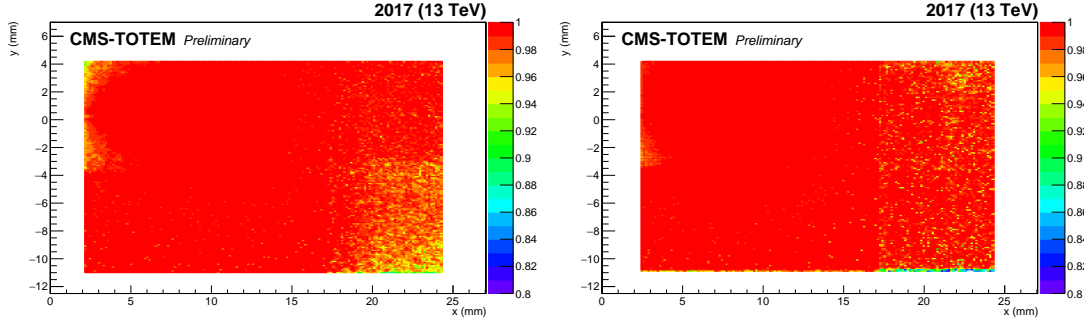
Figure 46: Pixel detector efficiency map, computed on the first data collected in 2017 and shown as a function of the global *x*-*y* coordinates. The slightly lower efficiency on the bottom-right corner of the sector 45 far station is due to non-optimal detector configuration.

In 2016, the near-far RPs correlation between inefficiency factors due to multiple tracks in strip detectors has been measured between 50% and 80%. The complete tracking inefficiency can therefore be computed as the product of the following factors: the multiple tracks inefficiencies (taking into account their correlation), the radiation damage inefficiency for both the near and far station, and the proton interaction probability. The latter has been measured by the TOTEM experiment to be approximately 2% (cf. Section 7.5.1 in Ref. [36]).

12.2 Pixel detector efficiency

The main contribution to the pixel detector inefficiency is given by radiation effects. The method used to derive the efficiency is described in detail in [41] and is based on the measurement of the efficiency of each detector plane during data-taking. A minimum bias sample collected at the beginning of the detector operation is used to model the track distribution; the track efficiency is quantified as the probability of having at least three efficient detector planes out of six.

The results are represented as a function of the global *x*-*y* coordinates on a scoring plane perpendicular to the beam, as in Figure 46. Statistical uncertainties have been estimated to be negligible with a toy Monte Carlo, and a 1% systematic uncertainty linked to the minimum bias sample choice has been assigned.

In 2017 and 2018 the efficiency *x*-*y* maps exhibit a small damaged region where the sensors are most irradiated[5], as shown in Figure 47. This region expands progressively with integrated luminosity. Outside the damaged region, the efficiency reaches a plateau higher than 98%. During each technical stop the RPs were shifted vertically by 0.5 mm, so as to spread the radiation damage over a wider region, and thus mitigate its effects.

Another effect can cause inefficiency in pixel detectors. If one of the protons coming from the interaction point interacts upstream of the near RPs, it can generate a shower of secondary particles. If the number of tracks exceeds the reconstruction capabilities of the pixels in the near RPs in 2018, a shower may cause the detectors to become inefficient.

This inefficiency factor has been quantified by studying the number of hits measured in pixel detectors. Since the track reconstruction algorithm fails if more than ten tracks are found, shower events are identified as events in which no tracks are reconstructed and the number of detected hits is significantly higher than that expected from detector noise.

The fraction of events identified as showers scales linearly with pileup, and is highly correlated,

---

[5]Inefficiency is actually due to the radiation damage of the electronics and not of the sensor itself.
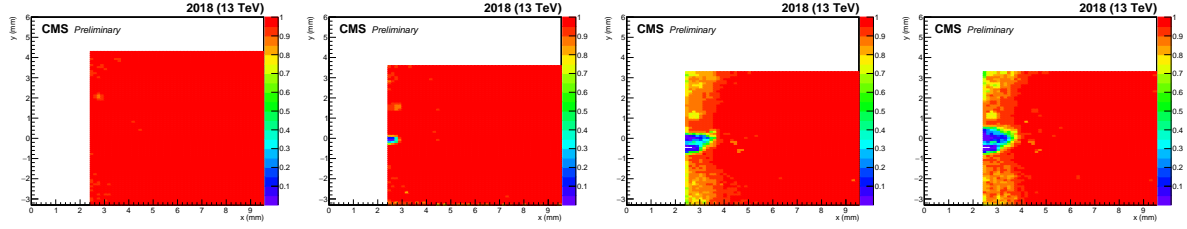
Figure 47: Evolution of the pixel detector package efficiency in the detector region closest to the beam for the sector 45 far station, computed with data collected in 2018. During each TS, detectors in both sectors were vertically shifted by 0.5 mm downwards. From left to right: efficiency computed after the detector collected $L_{INT} = 0$ fb^{-1}, $L_{INT} = 21.0$ fb^{-1}, $L_{INT} = 50.3$ fb^{-1}, $L_{INT} = 57.8$ fb^{-1}, respectively. Each efficiency map is produced using a small data sample of ~ 0.5fb^{-1}.

as expected, between the near and far detectors in the same sector. A conservative inefficiency upper limit of 1.5(1.7)% for sector 45(56) has been measured, with a 0.1% systematic uncertainty which accounts for the pileup dependency.

12.3 Multi-RP efficiency

The multiRP efficiency factor is evaluated in the same way in 2017 and 2018, and takes into account the efficiency of the detectors installed in the far RPs, the efficiency of the multiRP reconstruction algorithm, and the probability that a proton propagates from the near RPs to the far without interacting. These multiple components are evaluated together using a tag-and-probe method. For each data-taking period, minimum-bias samples have been selected for this purpose. Each single-RP proton reconstructed with the near RPs is used as tag, provided that its track angle measured with that tracking station is lower than 20 mrad. This selection excludes very inclined background tracks that do not originate from the interaction point.

The efficiency is evaluated as the ratio between the number of times in which a multi-RP proton is reconstructed using the single-RP tag proton, and the number of tag protons. The systematic uncertainties related to the sample choice for the efficiency estimation are $\approx 1\%$. Asymmetric statistical uncertainties are evaluated with the Clopper-Pearson frequentist approach [42].

The efficiency is plotted in Fig. 48 as a function of the *x-y* global coordinates of the 210-fr RP scoring plane. The overlap between the acceptances of the RPs in the same sector, combined with the collimator aperture limits, defines the shape of the efficiency map.

This efficiency has generally a plateau value higher than 90% in 2017, and slightly lower in 2018. These high values reflect the good performance of the detectors and of the reconstruction algorithm. Lower performance can be observed in the most irradiated region because of radiation damage and multiple tracks. The latter takes place when more than one track in the far RPs satisfies the association requirements with the near RPs track. Under these circumstances the multiRP reconstruction cannot choose between the far RP tracks, and fails, causing inefficiency.

Consistent results are observed in 2017 and 2018 when restricting the analysis to events with a single track in the near RP. A small loss in the 2018 multiRP reconstruction algorithm performance is observed when including events with multiple tracks in the near station, because of the higher multiple-match probability, as mentioned above.

Figure 49 shows, the fraction of reconstructed multi-RP protons predicted by the fast simulation, taking into account both efficiency and acceptance effects. The difference in the shape of the plots for the three years is mainly due to the different acceptance (see Fig. 32). The higher
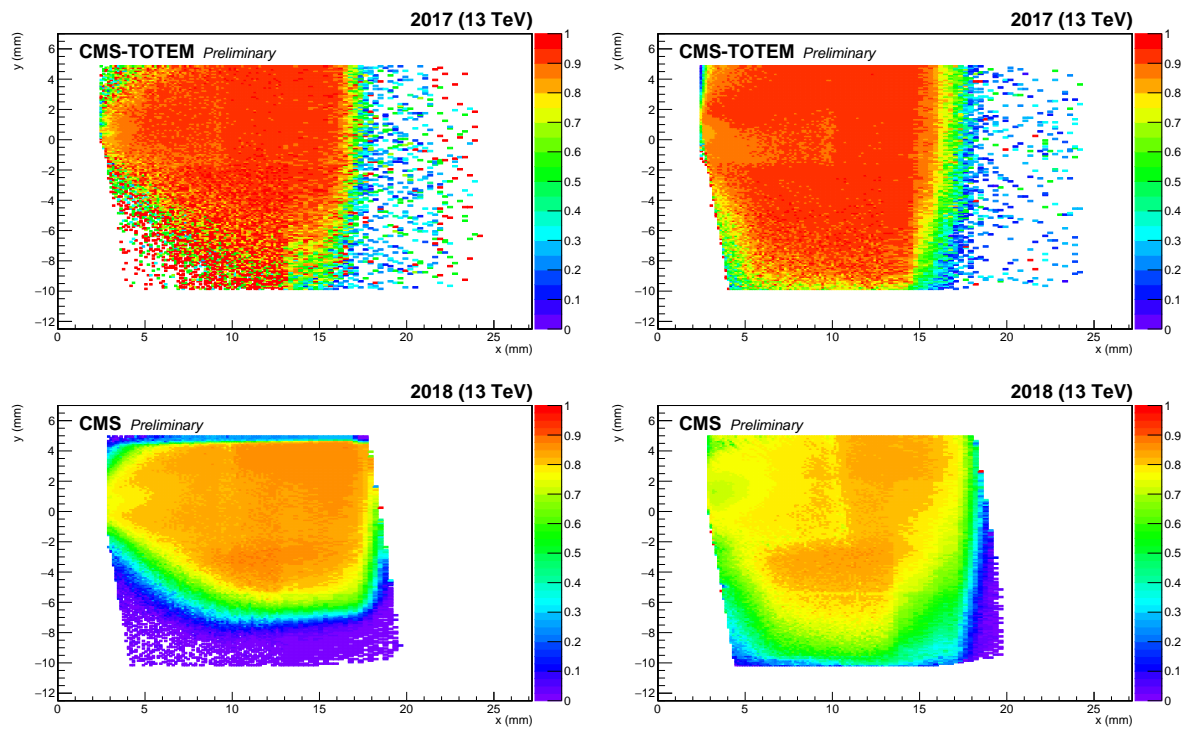
Figure 48: MultiRP efficiency factor that includes the efficiency of the detectors installed in the far RPs, the efficiency of the multiRP reconstruction algorithm, and the probability that a proton propagates from the near RPs to the far without interacting, shown as a function of the global *x*-*y* coordinates. Top: multiRP efficiency in both sectors at the beginning of the 2017 data-taking. Bottom: multiRP efficiency in both sectors at the beginning of the 2018 data-taking.

Figure 49: Fraction of reconstructed multiRP protons, as a function of ξ_{multi}, for a proton sample produced with the PPS fast simulation. Acceptance and efficiency effects are taken into account. The left and right plots show results 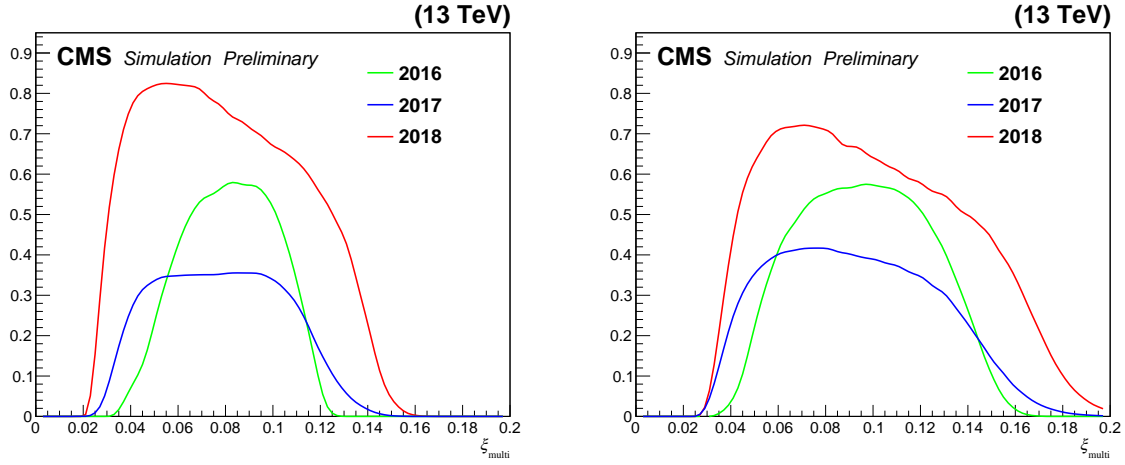for sector 45 and 56, respectively. The efficiency systematic uncertainties, computed combining in quadrature the systematics estimated for each efficiency factor, are 10%, 2.7%, and 2.1% for 2016, 2017, and 2018, respectively.

value of the fraction in 2018 reflects the presence of the pixel detectors (as opposed to the strip ones) in both RP stations.

The difference between the 2016 and 2017 performance is caused by multiple factors: the average pileup in 2017 was significantly higher than in 2016, producing a higher strip multi-tracking inefficiency (Fig. 44). The luminosity collected in 2016 was about one fourth than in 2017, making radiation damage less severe. Furthermore, the sector 45 near RP was not available for a significant portion of 2017 ($\approx$ 24% of the whole data-taking), thus effectively lowering the overall efficiency, as downtime is included as an inefficiency component.

13 Timing

In order to study the performance of the proton vertex matching provided by the PPS timing detectors, a special data set collected with low instantaneous luminosity is used, where the mean number of inelastic interactions per bunch crossing was $\mu \sim 1$. In this data set, a sample of events with exactly one reconstructed vertex built from a maximum of 10 tracks in the central CMS tracker and exactly one multi-RP proton on each arm of the PPS detectors is studied. This provides a control sample enriched in Central Diffraction (or Double Pomeron Exchange) events.

In signal events, the z position of the vertex as determined with the central CMS tracker, and the time-of-flight difference between the two protons (Δt_{PPS}) are linearly correlated with a slope of $c/2$ (where c is the speed of light). In practice, even in low-pileup data, there is a non-zero probability of combining unrelated pileup protons with the central vertex. Since the pileup protons are uncorrelated with the central vertex, this background may be modeled using event-mixing techniques, where either one or both protons are chosen from different events than that of the central vertex.

The correlation is quantified using a one-dimensional projection of $z_{\text{PPS,timing}} - z_{\text{vertex}}$, where $z_{\text{PPS,timing}} = \Delta t_{\text{PPS}} \times \frac{c}{2}$, and z_{vertex} is the position measured by the central tracker. To estimate the resolution for the signal events, a fit is performed to the sum of signal plus background,

using two Gaussian shapes. For the signal component, the mean and width of the Gaussian are left as free parameters. The resolution of z_{vertex} in the central tracker is estimated to be 50-150 μm for the selection applied here [43], and thus can be neglected.
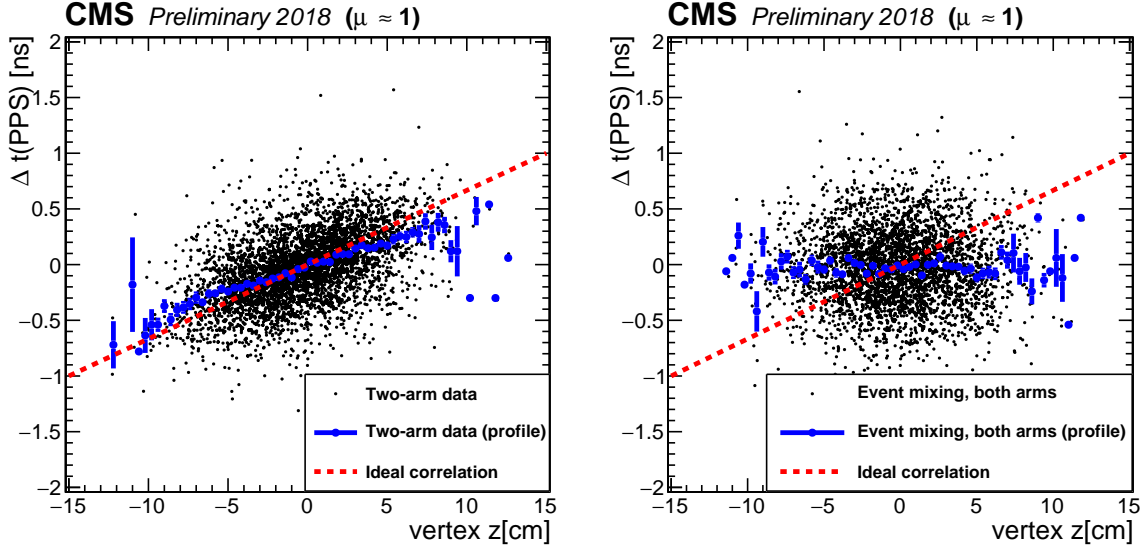

Figure 50: Correlation between the z vertex position measured in the central CMS tracker, and the time difference of the protons measured in the PPS detectors. Left: low-pileup data with protons on both arms. Right: mixed background sample, with both protons chosen from a different event than that of the central vertex. The red dashed line indicates the ideal slope of $c/2$, that would be expected with zero background.

To test the sensitivity to the background shape, three different approaches are tried. First, the background mean and width are treated as free parameters in the fit. Second, the mean and width are constrained from a fit to an event-mixing sample, where both protons are chosen from different events than that of the central vertex. Third, the mean and width are constrained from a fit to an event-mixing sample, where one proton is chosen from the same event as the central vertex, and the second proton is chosen from a different event.

The correlation between the vertex position and the proton time difference is shown in Fig. 50. The sample is further sub-divided into a "high resolution" selection, with < 100 ps timing resolution predicted on both arms (corresponding to the case with timing measurements on all 4 planes of each arm), and a "high efficiency" selection, with no requirement on the predicted timing resolution of each arm. The spatial resolutions obtained from the fits (Fig. 51) for the two categories are 1.87 ± 0.21 [$1.87 - 1.93$] cm and 2.77 ± 0.17 [$2.45 - 2.86$] cm, where the first value and uncertainty correspond to the central value and statistical uncertainty obtained using a Gaussian background shape with free parameters, and the numbers in brackets represent the range of central values obtained under the three different background approaches. The complete list of values obtained is shown in Table 8.

The resolutions obtained are consistent with the quadrature sum of single-arm timing resolutions, estimated independently [44]. This indicates that the overall vertex matching resolution is dominated by the single-arm detector and electronics performance, without large contributions correlated between the two arms. In the high resolution category, it confirms a time resolution below 100 ps per arm, with the full PPS timing system in LHC collisions. It further indicates that the single-arm resolutions may be used to predict the overall resolution in high-pileup data, where the two-arm technique described here cannot be used.
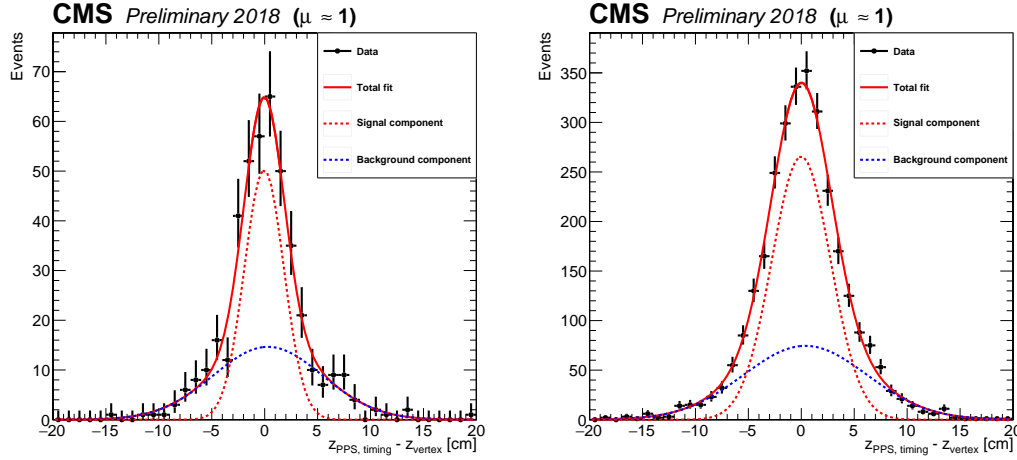
Figure 51: Vertex resolution obtained from the difference of proton arrival times, using data collected during low-pileup runs. Left: resolution for two-arm multi-RP events, using the subset of events with a predicted resolution < 100 ps for both arms. Right: resolution for two-arm events using all events with exactly one multi-RP proton on each arm. The fitted signal (red dashed line) and background (blue dashed line) are shown separately, with the means and widths of both components treated as free parameters.

Selection	Background	Resolution $\pm$ stat. [cm]
High resolution	Free	1.87 ± 0.21
High resolution	Both arms mixed	1.93 ± 0.18
High resolution	One arm mixed	1.92 ± 0.18
High efficiency	Free	2.77 ± 0.17
High efficiency	Both arms mixed	2.86 ± 0.10
High efficiency	One arm mixed	2.45 ± 0.13

Table 8: Vertex position resolutions obtained from the proton times measured in the PPS timing detectors, using different selection criteria and background shape assumptions. The sample of events in the high resolution and high efficiency categories is always the same, therefore the statistical uncertainties are highly correlated.

14 Summary

The procedures developed to reconstruct the proton tracks from the signals detected in the CMS Precision Proton Spectrometer have been described. The performance of the reconstruction has been studied with data from the LHC Run 2, with PPS collected data corresponding to an integrated luminosity larger than $110\,\text{fb}^{-1}$.

A multi-step alignment of the detectors is performed: alignment with respect to the LHC collimators, relative alignment of the sensor planes within an Roman Pot (RP) and among all RPs, global alignment with respect to the LHC beam with elastic events collected in low luminosity runs, and extrapolation to the high luminosity configuration. Finally, the timing detectors are aligned with respect to the tracking detectors. The alignment uncertainties are 150 μm and 100 μm in the horizontal and vertical projections, respectively. The precision of the relative alignment between near and far RPs is better than 10 μm.

A precise modelling of the LHC optics is a necessary precondition for the reconstruction. The track horizontal and vertical positions at the RPs can be obtained from the proton kinematics at

the interaction point via the so called optical functions. The horizontal dispersion optical function (D_x) is calibrated using the $L_y = 0$ constraint from the data and a sample of (semi)exclusive dimuon events. The horizontal dispersion carries information on the dependence of the optics model on the horizontal crossing angle. The parameters of the optics model (half crossing angle, quadrupole positions and magnet strengths) are determined from a fit to the beam position obtained from the beam position monitors and RPs, and the measured horizontal dispersion. The vertical dispersion is estimated from the vertical vertex position and the vertical scattering angle. The effective length optical function and its derivative with respect to the position along the beam are calibrated at $\xi = 0$ using elastic events.

An approximate determination of ξ and of the vertical scattering angle can be performed with the information of a single RP. A more accurate and complete determination of the proton kinematics is obtained by combining the information from both tracking RPs in each arm. The two reconstruction methods are referred to as single- and multi-RP. The single-RP reconstruction has significantly lower resolution especially because of the neglected term proportional to the horizontal scattering angle. A large bias at small and large ξ is hence observed given the asymmetric acceptance in the horizontal scattering angle. The multi-RP reconstruction has a much better resolution, negligible bias and comparable systematic uncertainties at small and intermediate ξ. At large ξ, the effect of the systematic uncertainty in the optics calibration is larger for the multi-RP reconstruction.

A fast simulation of the proton propagation along the beam line and of the PPS detectors has been developed; it includes realistic beam parameters and beam smearing effects, the calibrated optics model, the LHC aperture limitations, as well as the simulation of the detector planes and sensor geometry, acceptance and spatial resolution, and a realistic simulation of the proton arrival time.

A sample of (semi)exclusive dimuon events has been analyzed in order to validate the proton reconstruction. A good correlation between the measured proton ξ values and those inferred from the dimuon system is observed. The data are well described by the simulation. As expected, the multi-RP reconstruction shows a better resolution with respect to the single-RP method.

The proton reconstruction efficiency has been measured for the different data taking periods. It consists of different multiplicative factors describing the sensor efficiency, the reconstruction algorithm efficiency, and the effect of interactions along the proton path. The silicon strip detector efficiency is driven by radiation damage and multiple tracks in the same event. The silicon pixel detector efficiency is driven by the radiation damage. The effect of radiation damage is studied as a function of the integrated luminosity and is significant in the region closest to the detector edge facing the beam. The efficiency of the multi-RP reconstruction is smaller than that for the single-RP reconstruction, because of the sensor efficiency of the extra RP, and the effect of multiple, ambiguous proton combinations between tracks from the near and far detectors.

The correlation between the time of arrival difference of protons in the two detector arms and the z vertex position has been studied using low pileup data, enriched in central diffractive production. The width of the z position residuals is consistent with the single-arm timing resolutions. For part of the data taking period they are better than 100 ps, corresponding to ≈ 2 cm.

With its Run-2 operation, the CMS Precision Proton Spectrometer has proven the feasibility of continuously operating a near-beam proton spectrometer at a high luminosity hadron collider. PPS has had no impact on the operation of LHC in terms of background, heating, or

impedance. The success of PPS has been made possible by two independent collaborations, CMS and TOTEM, joining forces to pursue a common physics interest.

References

[1] CMS Collaboration, "The CMS experiment at the CERN LHC", *JINST* **3** (2008) S08004, `doi:10.1088/1748-0221/3/08/S08004`.

[2] TOTEM Collaboration, "The TOTEM experiment at the CERN Large Hadron Collider", *JINST* **3** (2008) S08007, `doi:10.1088/1748-0221/3/08/S08007`.

[3] CMS, TOTEM Collaboration, "CMS-TOTEM Precision Proton Spectrometer", Technical Report CERN-LHCC-2014-021, TOTEM-TDR-003, CMS-TDR-13, September, 2014.

[4] LHC Forward Physics Working Group Collaboration, "LHC Forward Physics", *J. Phys. G* **43** (2016) 110201, `doi:10.1088/0954-3899/43/11/110201`, `arXiv:1611.05079`.

[5] CMS Collaboration, "The CMS Precision Proton Spectrometer at the HL-LHC – Expression of Interest", `arXiv:arXiv:2103.02752v1`.

[6] E. Chapon, C. Royon, and O. Kepka, "Anomalous quartic WW gamma gamma, ZZ gamma gamma, and trilinear WW gamma couplings in two-photon processes at high luminosity at the LHC", *Phys. Rev. D* **81** (2010) 074003, `doi:10.1103/PhysRevD.81.074003`, `arXiv:0912.5161`.

[7] S. Fichet et al., "Light-by-light scattering with intact protons at the LHC: from Standard Model to New Physics", *JHEP* **02** (2015) 165, `doi:10.1007/JHEP02(2015)165`, `arXiv:1411.6629`.

[8] C. Baldenegro, S. Fichet, G. von Gersdorff, and C. Royon, "Searching for axion-like particles with proton tagging at the LHC", *JHEP* **06** (2018) 131, `doi:10.1007/JHEP06(2018)131`, `arXiv:1803.10835`.

[9] CMS Collaboration, "Performance of the CMS Level-1 trigger in proton-proton collisions at $\sqrt{s} = 13\,\text{TeV}$", *JINST* **15** (2020) P10017, `doi:10.1088/1748-0221/15/10/P10017`, `arXiv:2006.10165`.

[10] CMS Collaboration, "The CMS trigger system", *JINST* **12** (2017) P01020, `doi:10.1088/1748-0221/12/01/P01020`, `arXiv:1609.02366`.

[11] G. Ruggiero et al., "Characteristics of edgeless silicon detectors for the roman pots of the TOTEM experiment at the LHC", *Nuclear Instruments and Methods in Physics Research Section A: Accelerators, Spectrometers, Detectors and Associated Equipment* **604** (06, 2009) 242–245, `doi:10.1016/j.nima.2009.01.056`.

[12] TOTEM Collaboration, "Diamond Detectors for the TOTEM Timing Upgrade", *JINST* **12** (2017), no. 03, P03007, `doi:10.1088/1748-0221/12/03/P03007`, `arXiv:1701.05227`.

[13] V. Sola et al., "Ultra-Fast Silicon Detectors for 4D tracking", *JINST* **12** (2017), no. 02, C02072, `doi:10.1088/1748-0221/12/02/C02072`.

[14] O. S. Bruning et al., "LHC Design Report". CERN Yellow Reports: Monographs. CERN, Geneva, 2004. `doi:10.5170/CERN-2004-003-V-1`.

[15] H. Wiedemann, "Particle accelerator physics: Basic principles and linear beam dynamics". 1993.

[16] E. J. N. Wilson, "An introduction to particle accelerators". Oxford University Press, Oxford, 2001.

[17] TOTEM Collaboration, "LHC Optics Measurement with Proton Tracks Detected by the Roman Pots of the TOTEM Experiment", *New J. Phys.* **16** (2014) 103041, `doi:10.1088/1367-2630/16/10/103041,arXiv:1406.0546`.

[18] F. Nemes, "LHC optics determination with proton tracks measured in the CT-PPS detectors in 2016, before TS2", Technical Report CERN-TOTEM-NOTE-2017-002, Mar, 2017.

[19] F. Willeke and G. Ripken, "Methods of Beam Optics", *AIP Conf. Proc.* **184** (1989) 758, `doi:10.1063/1.38050`.

[20] G. Antchev et al., "Performance of the totem detectors at the lhc", *International Journal of Modern Physics A* **28** (2013), no. 31, 1330046, `doi:10.1142/S0217751X13300469`.

[21] CMS Collaboration, "Precision luminosity measurement in proton-proton collisions at $\sqrt{s} = 13$ TeV in 2015 and 2016 at CMS", *Eur. Phys. J. C* **81** (Apr, 2021) 800, `doi:10.1140/epjc/s10052-021-09538-2,arXiv:2104.01927`.

[22] CMS Collaboration, "CMS luminosity measurement for the 2017 data-taking period at $\sqrt{s} = 13$ TeV", technical report, CERN, Geneva, 2018.

[23] CMS Collaboration, "CMS luminosity measurement for the 2018 data-taking period at $\sqrt{s} = 13$ TeV", technical report, CERN, Geneva, 2019.

[24] J. Kašpar, "Elastic scattering at the LHC". PhD thesis, Charles U., 2011.

[25] TOTEM Collaboration, "Evidence for non-exponential elastic proton–proton differential cross-section at low $|t|$ and $\sqrt{s}$=8 TeV by TOTEM", *Nucl. Phys. B* **899** (2015) 527, `doi:10.1016/j.nuclphysb.2015.08.010,arXiv:1503.08111`.

[26] J. Kašpar, "Alignment of CT-PPS detectors in 2016, before TS2", Technical Report CERN-TOTEM-NOTE-2017-001, Mar, 2017.

[27] S. Fartoukh, "Experience with the ATS optics", in *7th Evian Workshop on LHC beam operation*, p. 93. CERN, Geneva, 2017.

[28] W. Herr, "Features and implications of different LHC crossing schemes", technical report, CERN, Geneva, Feb, 2003.

[29] H. Grote and F. Schmidt, "MAD-X: An upgrade from MAD8", *Conf. Proc. Particle Accelerator Conference,* **C030512** (2003) 3497.

[30] R. Billen and C. Roderick, "The LHC Logging Service: Capturing, storing and using time-series data for the world's largest scientific instrument", Technical Report AB-Note-2006-046. CERN-AB-Note-2006-046, CERN, Nov, 2006.

[31] C. Roderick and R. Billen, "The LSA Database to Drive the Accelerator Settings", Technical Report CERN-ATS-2009-100, CERN, Geneva, Nov, 2009.

[32] N. Aquilina et al., "The FiDel model at 7 TeV", Technical Report CERN-ACC-2014-0092, Jun, 2014.

[33] F. J. Nemes, "Elastic scattering of protons at the TOTEM experiment at the LHC". PhD thesis, Eotvos U., 2015.

[34] CMS, TOTEM Collaboration, "Observation of proton-tagged, central (semi)exclusive production of high-mass lepton pairs in pp c ollisions at 13 TeV with the CMS-TOTEM precision proton spectrometer", *JHEP* **07** (2018) 153, `doi:10.1007/JHEP07(2018)153,arXiv:1803.04496`.

[35] F. James and M. Roos, "Minuit: A System for Function Minimization and Analysis of the Parameter Errors and Correlations", *Comput. Phys. Commun.* **10** (1975) 343, `doi:10.1016/0010-4655(75)90039-9`.

[36] H. Niewiadomski, "Reconstruction of protons in the TOTEM roman pot detectors at the LHC". PhD thesis, Manchester U., 2008.

[37] L. Evans and P. Bryant, "LHC Machine", *JINST* **3** (2008) S08001, `doi:10.1088/1748-0221/3/08/S08001`.

[38] ATLAS Collaboration, "Observation and Measurement of Forward Proton Scattering in Association with Lepton Pairs Produced via the Photon Fusion Mechanism at ATLAS", *Phys. Rev. Lett.* **125** (2020), no. 26, 261801, `doi:10.1103/PhysRevLett.125.261801`, `arXiv:2009.14537`.

[39] CMS and TOTEM Collaboration, "Efficiency of Si-strips sensors used in Precision Proton Spectrometer", Technical Report CMS-DP-2018-056, CERN, Sep, 2018.

[40] CMS Collaboration, "Efficiency of the Si-strips sensors used in the Precision Proton Spectrometer: radiation damage", Technical Report CMS-DP-2019-035, CERN, Oct, 2019.

[41] CMS Collaboration, "Efficiency of the Pixel sensors used in the Precision Proton Spectrometer: radiation damage", Technical Report CMS-DP-2019-036, CERN, Oct, 2019.

[42] C. J. Clopper and E. S. Pearson, "The use of confidence or fiducial limits illustrated in the case of the binomial", *Biometrika* **26** (1934), no. 4, 404.

[43] CMS Collaboration, "Description and performance of track and primary-vertex reconstruction with the CMS tracker", *JINST* **9** (2014), no. 10, P10009, `doi:10.1088/1748-0221/9/10/P10009,arXiv:1405.6569`.

[44] CMS Collaboration, "Time resolution of the diamond sensors used in the Precision Proton Spectrometer", Technical Report CMS-DP-2019-034, CERN, Oct, 2019.